Monopolar Acoustic Pulses in Histotripsy and Other Applications

by

Yige Li

A dissertation submitted in partial fulfillment
of the requirements for the degree of
Doctor of Philosophy
(Biomedical Engineering)
in the University of Michigan
2019

Doctoral Committee:

Professor Charles A. Cain, Chair
Associate Research Scientist Timothy Hall
Research Professor Luis Hernandez-Garcia
Associate Professor Zhen Xu

Yige Li

yigeli@umich.edu

ORCID iD: 0000-0002-4685-5384

Dedication

To my parents, Zhongxian and Cuiling, who have encouraged me to chase my goals and supported me during my many years as a student, and to my girlfriend, Mengyao, who has always been there for me.

Acknowledgements

I would like first to express my gratitude to my advisor, Charles, who has been such a great mentor for me during my years as a graduate student. Since I arrived at Michigan, I've started the most unforgettable journey of my life. His endless passion for research has always inspired me to think deeply. His patient guidance has allowed me to learn and work at my own pace. His great attention to detail has taught me that good work comes from a sense of responsibility. I'd also like to thank all the other members of my dissertation committee for providing me with suggestions and feedback during my study. Luis has provided valuable insights on some innovative projects we collaborated on. I've also benefitted greatly from Tim's advice and guidance on uncountable questions during my experiments in the lab. Zhen's dedication to work has always inspired me to have a plan and execute it the best I can.

I would also like to thank all the other lab members, whom I learn from and grow with: Jon Sukovich, Hedieh, Jon Lundt, Tyler, Jon Macoskey, Aiwei, Tejaswi, Sang, Ryan, Ning, Ellen, Greyson, Zhijie, and Varsha. I learn so much from the conversation and discussion we've had throughout theses years, no matter academic or about life. The working environment here feels like a family because of you all.

I would also like to thank all the former graduate students, who helped me so much especially during my junior years: Kuang-Wei, Xi, Yohan, Steven, Eli, Alex, and Ryan. Your experience and suggestions helped me go through a lot of difficulties.

Finally, I would like to thank my parents, who have always encouraged me to chase what I want to achieve and supported me all these years without me being around with them. My

girlfriend, Mengyao, is always there for me no matter what happens. I'd like to thank her for always caring about my feelings and sharing with me joy and laughter.

Table of Contents

List of Tables

List of Figures

Abstract

Monopolar acoustic pulses decouple the compressional (positive) and rarefactional (negative) half-cycles within acoustic bursts and could be crucial for many applications. In this work, a frequency compounding transducer was designed and built to generate pseudo-monopolar peak positive pulses and peak negative pulses. The transducer consisted of 113 individual piezoelectric elements with 7 various resonant frequencies. Focal waveforms of both peak positive pulses and peak negative pulses were measured. Different pulsing sequences were then designed and applied for studying several aspects of histotripsy. First off, the use of pseudo-monopolar pulses with variable, controllable delays could achieve a new technique called "enhanced shock scattering histotripsy". The shock scattering process in normal shock scattering histotripsy might not be optimal because it involves a complex interaction between positive and negative phases within an acoustic pulse to initiate a robust cavitation bubble cloud. With enhanced shock scattering histotripsy, we aimed to generate cavitation bubble clouds by shock scattering with mostly peak positive pulses. Observations of bubble clouds generated by this technique were achieved by using high-speed photography. For example, 16 successive bubble clouds were generated by 16 peak positive pulses following an initial peak negative pulse. The feasibility of the technique was tested by generating a precise lesion in a red-blood-cell phantom. Additional efforts were made to investigate the cavitation thresholds at pressure-release interfaces by applying pseudo-monopolar peak positive pulses with various pressure levels. Different interface models were explored. Threshold curves showed that the thresholds at interfaces were less than 20 MPa negative, which was lower than the intrinsic threshold in free

water. They also varied with spatial locations for certain materials. Another potential application of high amplitude monopolar pulses is ultrasonic neural stimulation. Preliminary work was done where we hypothesized the generation of de-modulated low frequency currents from simultaneous ultrasound and high frequency, oscillating magnetic fields. Varying the two frequencies by a few kHz could produce a de-modulated, difference-frequency current similar to that generated by Transcranial Magnetic Stimulation. The pressure field generated by a 500 kHz ultrasound transducer and the resultant current density magnitude distribution in the presence of a magnetic field were simulated. Experimentally, with same conditions, currents of 0.34 μA/cm^2 at 4 kHz and 0.39 μA/cm^2 at 3 kHz were detected, which matched the simulation results.

Chapter 1 Introduction

This dissertation focuses on the design and build of a new frequency compounding transducer to generate monopolar acoustic pulses which can be useful for various applications. After being successfully generated, monopolar pulses are applied within unique pulsing sequences to enhance shock scattering histotripsy. Efforts are also made to investigate the cavitation thresholds at pressure-release interfaces with monopolar peak positive pulses. Some specific safety issues associated with positive acoustic pressures are addressed as well. This dissertation also presents the study where localized currents were generated by applying simultaneous ultrasound and oscillating magnetic fields, which could lead to the development of a novel non-invasive brain stimulation method that could benefit greatly from the generation of monopolar pulses.

1.1 Shock Scattering Histotripsy

Shock scattering histotripsy is a noninvasive ultrasound therapy that uses very short, high-pressure ultrasound pulses to generate robust cavitation clouds to achieve mechanical tissue fractionation. A traditional shock scattering histotripsy pulse consists of 3 to 20 cycles with multiple compressional (positive) and rarefactional (negative) half-cycles that must interact with each other to produce therapeutically effective bubble clouds in a predictable and controllable manner[1-6], attributes not usually associated with cavitation phenomena. To work properly, the peak pressure magnitude of the negative half cycles should exceed about 15 MPa (negative) and the positive half-cycles should be reasonably well-developed shock fronts exceeding about 30 MPa (positive). Mechanistically, Maxwell et al.[7] showed that initial negative half-cycles of a

histotripsy pulse can generate incidental bubbles which act as pressure-release surfaces from which the positive shock fronts are scattered. Incidental bubbles are single bubbles that are sparsely concentrated and can be generated by multiple sub-intrinsic threshold negative pulses, whose negative pressures (e.g. 18 MPa) are below an intrinsic threshold of about 26 to 30 MPa (negative), based on previous studies[8-10]. The incidental bubbles are likely seeded from the pre-existing dissolved sub-micrometer gas bubbles or weak pockets[9]. The scattering process inverts the positive shock fronts that now propagate back towards the transducer and add constructively with the next counter propagating negative half-cycle of the histotripsy pulse. If this composite waveform exceeds the intrinsic threshold, therapeutically effective dense energetic bubble clouds are generated at the focus. Alternatively, for very short histotripsy pulses (less than 2 cycles), a dense cavitation cloud can be initiated directly when the peak negative pressure exceeds the intrinsic threshold. This "intrinsic threshold histotripsy" approach usually gives superior results because very dense bubble clouds can be generated precisely in the region where the local negative pressure exceeds the intrinsic threshold. But, the threshold often cannot be achieved when the target volume is deep with an entry window which restricts the usable transducer aperture. Shock scattering histotripsy then becomes one of the alternatives that can be used. Much longer pulses at lower peak intensities can produce therapeutically effective bubble clouds by producing high temperatures close to the boiling point. Thus, "boiling histotripsy" is another approach when peak intensities that can be reached in the target volume are limited[11-13]. Cavitation bubble cloud due to the backscattering of HIFU from a laser-induced bubble was studied by Ogasawara et al.[14]. Yoshizawa et al. demonstrated control of shock scattering cavitation clouds with positive enhanced and negative enhanced waveforms, which were

achieved by applying dual-frequency ultrasound sequences[15]. Shock scattering histotripsy in other contexts has been studied by several other groups[16-22].

1.2 Monopolar Acoustic Pulses and Frequency Compounding

The generation of monopolar acoustic pulses is an enabling technology since it could be useful for various applications. First, it could be used to enhance shock scattering histotripsy since it could potentially greatly reduce the number of negative pressures applied which could help reduce pre-focal cavitation at tissue interfaces in the propagation path. Also, it could be used to investigate the cavitation thresholds at interfaces. Studying safety issues associated with positive acoustic pressures could also benefit from the generation of monopolar positive pulses. Not just limited to histotripsy, the generation of monopolar acoustic pulses could also be useful for non-invasive neural stimulation. One possibility is that high-amplitude monopolar peak positive pulses could be used to provide high-pressure ultrasound fields without creating cavitation to eventually induce localized currents strong enough to achieve neural stimulation. This process of generating a localized current involves applying an appropriate magnetic field simultaneously with the ultrasound. Another possibility is that high-amplitude monopolar peak positive pulses could be used to directly achieve non-invasive neural stimulation by causing mechanical deformation on certain ion channels to eventually trigger action potentials. For imaging purposes, the generation of monopolar acoustic pulses could help improve axial resolution and reduce speckles.

In our work, we propose to design and build a frequency compounding transducer to generate monopolar acoustic pulses, and then focus on using them to investigate several aspects of histotripsy and conduct some preliminary work for developing an innovative brain stimulation method.

The generation of monopolar acoustic pulses can be achieved by using the concept of frequency compounding. By adjusting time delays of individual frequency components to allow their principal peak positive pressure (P+) to align temporally, high-pressure peak positive pulses are generated by constructive addition or compounding. Destructive interference occurs outside the peak-positive-overlapped temporal window, resulting in a good approximation of a pseudo-monopolar (nearly half-cycle) pulse with a sharp high-pressure positive phase and low-amplitude, temporally smeared out negative phase. A similar pseudo-monopolar pulse with a sharp dominant negative phase can be generated in a similar way by constructive compounding of all principal peak negative pressure (P-) pulses from all the elements.

"Unipolar" pulses generated by optimizing the electrical excitation signal of a piezoelectric transducer were explored by Rougny et al.[23] and Sferruzza et al.[24, 25]. Bailey et al. used an electrohydraulic lithotripter to generate positive pressure pulses and negative pressure pulses and studied the bioeffects of those pulses in vivo[26]. The generation of pseudo-monopolar peak positive pulses and peak negative pulses based on the concept of frequency compounding was investigated by Lin et al.[27]. Previous studies also investigated frequency compounding as a method for speckle reduction in ultrasound images[28-31] and optical coherence tomography [32]; however, the compounding is done at the level of image frames, not the imaging pulses, each of which has a different center frequency.

1.3 Brain Stimulation and Electrical Currents Generated Based on the Lorentz Force Effect

Non-invasive brain stimulation has been widely studied not only for the treatment of psychiatric and neurological disorders, but also for research purposes such as mapping brain neural networks. Induced neural activities have shown effectiveness for depression[33],

Alzheimer's disease[34] and Parkinson's disease[35]. However, currently existing techniques that could achieve non-invasive brain stimulation have obvious drawbacks. One of those is that the stimulation lacks penetration depth into the brain for methods such as the Transcranial Magnetic Stimulation (TMS)[36, 37]. Also, the stimulation region is not highly localized and well-controlled due to the characteristics of the magnetic fields. Brain stimulation is useful for research into brain networks as well. For example, deep brain stimulation has been used to study neural activities in memory circuits, including the hippocampal areas[38].

Monopolar acoustic pulses could be crucial for the development of novel non-invasive brain stimulation methods since they could give us high positive pressure with a minimal negative pressure, i.e., we could get high positive pressure without exceeding the mechanical index (MI) limitation in diagnostic ultrasound. This will not only be useful for studying direct ultrasound brain stimulation, which have been reported by previous studies[39-41], but also benefit other potential innovative modalities such as the method that combines ultrasound and magnetic field to generate electrical currents to achieve neural stimulation, which will be focused on in this work.

The idea of combining ultrasound and magnetic fields to generate electrical currents using the Lorentz force phenomenon has been proposed before[42-45]. The Lorentz force principle states that charges moving in the presence of a magnetic field will experience a force that is perpendicular to both the magnetic field and the direction of the particles' movement. Ultrasound waves consist of oscillating pressure fields that cause the particles in a medium to move in an oscillatory fashion (particle velocity). Thus, in an ionic solution where ultrasound is propagating, moving charged particles will experience a Lorentz force in the presence of a magnetic field. The

force will push the positively charged particles in one direction while push the negatively charged particles in the opposite direction, resulting in a net ionic current.

Different research groups have been able to detect electrical current signals based on the Lorentz force phenomenon, although their goals and utilities varied. For instance, A. Montalibet et al. used the principle to make conductivity measurements of biological media[42]. Later on, some studies investigated the possibility of performing electrical impedance tomography (EIT) based on the principle[43, 46, 47]. Norton proposed the idea of using the induced currents to achieve brain stimulation[42]. Yuan et al. later conducted a simulation study of the technique, which they called Transcranical Magneto-Acoustical Stimulation (TMAS), with the Hodgkin-Huxley neuron model[41]. In all the studies mentioned above, a constant, static magnetic field was applied, which meant that the induced currents oscillated at the same frequency as the ultrasound waves. However, high frequency currents usually have little effect on generating action potentials of an axon or neuron given its capacitance of the membrane, whereas, quasi-static currents are needed to generate action potentials. For example, the active cycle of the induced currents is about 0.3 msec (corresponding to 3 kHz to 4 kHz in frequency), in the range of a TMS pulse[37].

1.4 Organization of the Dissertation

In Chapter 1, the significance of the generation of monopolar ultrasound pulses is addressed. Then, the mechanism of shock scattering histotripsy and the concept of frequency compounding are reviewed. Also, several studies about localized currents generated by the Lorentz force effect are reviewed. In Chapter 2, the design of a new frequency compounding transducer is described, and focal waveforms of monopolar acoustic pulses are presented. In Chapter 3, experiments of enhanced shock scattering histotripsy with pseudo-monopolar ultrasound pulses are conducted. In the following chapter, cavitation thresholds at pressure-

release interfaces are investigated and threshold curves with different interface materials are presented. Chapter 5 addresses a novel technique of generating de-modulated currents with simultaneous ultrasound and oscillating magnetic fields. Finally, Chapter 6 summarizes the work and discusses future work on enhanced shock scattering histotripsy, cavitation at pressure-release interfaces, and localized currents by ultrasound and magnetic fields.

1.5 References

1. Xu Z, Ludomirsky A, Eun LY, Hall TL, Tran BC, Fowlkes JB, Cain CA. Controlled ultrasound tissue erosion. IEEE transactions on ultrasonics, ferroelectrics, and frequency control. 2004 Jun;51(6):726-36.

2. Roberts WW, Hall TL, Ives K, Wolf Jr JS, Fowlkes JB, Cain CA. Pulsed cavitational ultrasound: a noninvasive technology for controlled tissue ablation (histotripsy) in the rabbit kidney. The Journal of urology. 2006 Feb 1;175(2):734-8.

3. Xu Z, Raghavan M, Hall TL, Chang CW, Mycek MA, Fowlkes JB, Cain CA. High speed imaging of bubble clouds generated in pulsed ultrasound cavitational therapy-histotripsy. IEEE transactions on ultrasonics, ferroelectrics, and frequency control. 2007 Oct;54(10):2091-101.

4. Xu Z, Hall TL, Fowlkes JB, Cain CA. Effects of acoustic parameters on bubble cloud dynamics in ultrasound tissue erosion (histotripsy). The Journal of the Acoustical Society of America. 2007 Jul;122(1):229-36.

5. Xu Z, Raghavan M, Hall TL, Mycek MA, Fowlkes JB, Cain CA. Evolution of bubble clouds induced by pulsed cavitational ultrasound therapy-histotripsy. IEEE transactions on ultrasonics, ferroelectrics, and frequency control. 2008 May;55(5).

6. Maxwell AD, Cain CA, Duryea AP, Yuan L, Gurm HS, Xu Z. Noninvasive thrombolysis using pulsed ultrasound cavitation therapy–histotripsy. Ultrasound in medicine & biology. 2009 Dec 1;35(12):1982-94.

7. Maxwell AD, Wang TY, Cain CA, Fowlkes JB, Sapozhnikov OA, Bailey MR, Xu Z. Cavitation clouds created by shock scattering from bubbles during histotripsy. The Journal of the Acoustical Society of America. 2011 Oct;130(4):1888-98.

8. Maxwell AD, Cain CA, Hall TL, Fowlkes JB, Xu Z. Probability of cavitation for single ultrasound pulses applied to tissues and tissue-mimicking materials. Ultrasound in medicine & biology. 2013 Mar 1;39(3):449-65.

9. Lin KW, Duryea A, Kim Y, Hall T, Xu Z, Cain C. Dual-beam histotripsy: A low-frequency pump enabling a high-frequency probe for precise lesion formation. IEEE transactions on ultrasonics, ferroelectrics, and frequency control. 2014 Feb;61(2):325-40.

10. Lin KW, Kim Y, Maxwell AD, Wang TY, Hall TL, Xu Z, Fowlkes JB, Cain C. Histotripsy beyond the intrinsic cavitation threshold using very short ultrasound pulses: Microtripsy. IEEE transactions on ultrasonics, ferroelectrics, and frequency control. 2014 Feb;61(2):251-65.

11. Simon JC, Sapozhnikov OA, Khokhlova VA, Wang YN, Crum LA, Bailey MR. Ultrasonic atomization of tissue and its role in tissue fractionation by high intensity focused ultrasound. Physics in Medicine & Biology. 2012 Nov 16;57(23):8061.

12. Wang YN, Khokhlova T, Bailey M, Hwang JH, Khokhlova V. Histological and biochemical analysis of mechanical and thermal bioeffects in boiling histotripsy lesions induced by high intensity focused ultrasound. Ultrasound in medicine & biology. 2013 Mar 1;39(3):424-38.

13. Khokhlova TD, Haider YA, Maxwell AD, Kreider W, Bailey MR, Khokhlova VA. Dependence of boiling histotripsy treatment efficiency on HIFU frequency and focal pressure levels. Ultrasound in medicine & biology. 2017 Sep 1;43(9):1975-85.

14. Ogasawara T, Horiba T, Sano T, Takahira H. Pressure measurement and high-speed observation on the cavitation bubble cloud due to the backscattering of HIFU from a laser-induced bubble. Fluid Dynamics Research. 2018 Nov 7;50(6):065512.

15. Yoshizawa S, Takagi R, Umemura SI. Enhancement of high-intensity focused ultrasound heating by short-pulse generated cavitation. Applied Sciences. 2017;7(3):288.

16. Xu J, Bigelow TA. Experimental investigation of the effect of stiffness, exposure time and scan direction on the dimension of ultrasound histotripsy lesions. Ultrasound in medicine & biology. 2011 Nov 1;37(11):1865-73.

17. Xu J, Bigelow TA, Riesberg GM. Impact of preconditioning pulse on lesion formation during high-intensity focused ultrasound histotripsy. Ultrasound in medicine & biology. 2012 Nov 1;38(11):1918-29.

18. Xu J, Bigelow TA, Lee H. Effect of pulse repetition frequency and scan step size on the dimensions of the lesions formed in agar by HIFU histotripsy. Ultrasonics. 2013 Apr 1;53(4):889-96.

19. Xu J, Bigelow TA, Davis G, Avendano A, Shrotriya P, Bergler K, Hu Z. Dependence of ablative ability of high-intensity focused ultrasound cavitation-based histotripsy on mechanical properties of agar. The Journal of the Acoustical Society of America. 2014 Dec;136(6):3018-27.

20. Bader KB, Crowe MJ, Raymond JL, Holland CK. Effect of frequency-dependent attenuation on predicted histotripsy waveforms in tissue-mimicking phantoms. Ultrasound in medicine & biology. 2016 Jul 1;42(7):1701-5.

21. Bader KB, Haworth KJ, Shekhar H, Maxwell AD, Peng T, McPherson DD, Holland CK. Efficacy of histotripsy combined with rt-PA in vitro. Physics in Medicine & Biology. 2016 Jun 29;61(14):5253.

22. Bader KB, Holland CK. Predicting the growth of nanoscale nuclei by histotripsy pulses. Physics in Medicine & Biology. 2016 Mar 17;61(7):2947.

23. Rougny E, Chapelon JY, Querleux B, Leveque JL, Cathignol D. The use of a thick focused piezoelectric transducer to generate short duration unipolar wave. In Acoustical Imaging 1992 (pp. 283-287). Springer, Boston, MA.

24. Sferruzza JP, Birer A, Theillere Y, Cathignol D. Generation of high power unipolar pulse with a piezocomposite transducer. InUltrasonics Symposium, 1999. Proceedings. 1999 IEEE 1999 (Vol. 2, pp. 1125-1128). IEEE.

25. Sferruzza JP, Birer A, Matias A, Theillère Y, Cathignol D. Experimental identification of a piezoelectric material for high impulse pressure wave applications. Sensors and Actuators A: Physical. 2001 Feb 15;88(2):146-55.

26. Bailey MR, Dalecki D, Child SZ, Raeman CH, Penney DP, Blackstock DT, Carstensen EL. Bioeffects of positive and negative acoustic pressures in vivo. The Journal of the Acoustical Society of America. 1996 Dec;100(6):3941-6.

27. Lin KW, Hall T, McGough R, Xu Z, Cain C. Synthesis of monopolar ultrasound pulses for therapy: The frequency-compounding transducer. IEEE transactions on ultrasonics, ferroelectrics, and frequency control. 2014 Jul;61(7):1123-36.

28. Magnin PA, von Ramm OT, Thurstone FL. Frequency compounding for speckle contrast reduction in phased array images. Ultrasonic imaging. 1982 Jul;4(3):267-81.

29. Shankar PM, Newhouse VL. Speckle reduction with improved resolution in ultrasound images. IEEE transactions on Sonics and Ultrasonics. 1985 Jul;32(4):537-43.

30. Trahey GE, Allison JW, Smith SW, Von Ramm OT. A quantitative approach to speckle reduction via frequency compounding. Ultrasonic Imaging. 1986 Jul;8(3):151-64.

31. Adam D, Beilin-Nissan S, Friedman Z, Behar V. The combined effect of spatial compounding and nonlinear filtering on the speckle reduction in ultrasound images. Ultrasonics. 2006 Feb 1;44(2):166-81.

32. Pircher M, Götzinger E, Leitgeb RA, Fercher AF, Hitzenberger CK. Speckle reduction in optical coherence tomography by frequency compounding. Journal of Biomedical Optics. 2003 Jul;8(3):565-70.

33. Mayberg HS, Lozano AM, Voon V, McNeely HE, Seminowicz D, Hamani C, Schwalb JM, Kennedy SH. Deep brain stimulation for treatment-resistant depression. Neuron. 2005 Mar 3;45(5):651-60.

34. Cotelli M, Calabria M, Manenti R, Rosini S, Zanetti O, Cappa SF, Miniussi C. Improved language performance in Alzheimer disease following brain stimulation. Journal of Neurology, Neurosurgery & Psychiatry. 2011 Jul 1;82(7):794-7.

35. Deuschl G, Schade-Brittinger C, Krack P, Volkmann J, Schäfer H, Bötzel K, Daniels C, Deutschländer A, Dillmann U, Eisner W, Gruber D. A randomized trial of deep-brain stimulation for Parkinson's disease. New England Journal of Medicine. 2006 Aug 31;355(9):896-908.

36. Grisaru N, Chudakov B, Yaroslavsky Y, Belmaker RH. Transcranial magnetic stimulation in mania: a controlled study. American Journal of Psychiatry. 1998 Nov 1;155(11):1608-10.

37. Wagner T, Gangitano M, Romero R, Théoret H, Kobayashi M, Anschel D, Ives J, Cuffin N, Schomer D, Pascual-Leone A. Intracranial measurement of current densities induced by transcranial magnetic stimulation in the human brain. Neuroscience letters. 2004 Jan 9;354(2):91-4.

38. Laxton AW, Tang-Wai DF, McAndrews MP, Zumsteg D, Wennberg R, Keren R, Wherrett J, Naglie G, Hamani C, Smith GS, Lozano AM. A phase I trial of deep brain stimulation of memory circuits in Alzheimer's disease. Annals of neurology. 2010 Oct;68(4):521-34.

39. Kim H, Chiu A, Lee SD, Fischer K, Yoo SS. Focused ultrasound-mediated non-invasive brain stimulation: examination of sonication parameters. Brain stimulation. 2014 Sep 1;7(5):748-56.

40. Yang T, Chen J, Yan B, Zhou D. Transcranial ultrasound stimulation: a possible therapeutic approach to epilepsy. Medical hypotheses. 2011 Mar 1;76(3):381-3.

41. Mueller J, Legon W, Opitz A, Sato TF, Tyler WJ. Transcranial focused ultrasound modulates intrinsic and evoked EEG dynamics. Brain stimulation. 2014 Nov 1;7(6):900-8.

42. Montalibet A, Jossinet J, Matias A, Cathignol D. Electric current generated by ultrasonically induced Lorentz force in biological media. Medical and Biological Engineering and Computing. 2001 Jan 1;39(1):15-20.

43. Ammari H, Grasland-Mongrain P, Millien P, Seppecher L, Seo JK. A mathematical and numerical framework for ultrasonically-induced Lorentz force electrical impedance tomography. Journal de Mathematiques Pures et Appliquées. 2015 Jun 1;103(6):1390-409.

44. Yuan Y, Chen Y, Li X. Theoretical analysis of transcranial magneto-acoustical stimulation with Hodgkin-Huxley neuron model. Frontiers in computational neuroscience. 2016 Apr 19;10:35.

45. Norton SJ. Can ultrasound be used to stimulate nerve tissue?. Biomedical engineering online. 2003 Dec;2(1):6.

46. Grasland-Mongrain P, Mari JM, Chapelon JY, Lafon C. Lorentz force electrical impedance tomography. Irbm. 2013 Nov 1;34(4-5):357-60.

47. Grasland-Mongrain P, Destrempes F, Mari JM, Souchon R, Catheline S, Chapelon JY, Lafon C, Cloutier G. Acousto-electrical speckle pattern in Lorentz force electrical impedance tomography. Physics in Medicine & Biology. 2015 Apr 23;60(9):3747.

Chapter 2 Frequency Compounding Transducer and Monopolar Ultrasound Pulses

Using the concept of frequency compounding to generate monopolar ultrasound pulses was investigated by Lin et al[1]. A relatively small and hemisphere frequency compounding transducer was built, and pseudo-monopolar peak positive pulses and peak negative pulses were successfully generated. However, being relatively small and in a hemisphere geometry, the transducer limits our ability to conduct further experiments since the operation window around the focus is very limited and not open.

In our study, we propose to design and build a new frequency compounding transducer with a bigger aperture and a higher F-number so that we have a completely open operation window as well as several other improvements, which will be discussed later in this chapter. This new frequency compounding transducer allows us to perform series of experiments we aim to do.

2.1 Frequency Compounding Transducer and Generation of Pseudo-Monopolar Pulses

2.1.1 Methods: Design and Manufacturing of Frequency Compounding Transducer

The frequency compounding transducer (Figure 2.1) consists of 113 individual piezoelectric elements with 7 various resonant frequencies. The frequencies used are 250 kHz (39 elements), 500 kHz (17 elements), 750 kHz (10 elements), 1 MHz (19 elements), 1.5 MHz (6 elements), 2 MHz (10 elements), and 3 MHz (12 elements). Each 250-kHz element consists of two 500-kHz, 20-mm-diameter piezoelectric discs (PZ36, Ferroperm, Kvistgaard, Denmark) bonded together with epoxy (LOCTITE E-00NS, Henkel, Dusseldorf, Germany). Each 250-kHz

element consists of two 500 kHz, 20-mm-diameter piezoelectric discs. Each 500-kHz element consists of two 1 MHz, 20-mm-diameter piezoelectric discs. All higher frequencies use single 20-mm-diameter piezoelectric discs (PZ36, Ferroperm). The selection of the frequencies, the number of elements used for each frequency, and the relative ratio of pressure outputs among all frequencies were optimized by a Monte-Carlo-method-based optimization program in Matlab. Pseudo-random combinations were generated by the program, each of which resulted in a frequency-compounded acoustic pulse. Then, parameters including the peak pressure level and the peak positive (P+) over peak negative (P-) ratio were examined. Also, the overall shape of the compounded pulse was considered. We decided the combination of frequencies, element numbers and the relative ratio of pressure outputs upon obtaining a satisfactory overall waveform that met all the requirements mentioned earlier. The optimization was mainly done for generating monopolar peak positive pulses. Monopolar peak negative pulses resulting from the optimized combination were good enough since by inverting the polarity of the excitation signals, the individual short pulses were highly symmetrical to those generated for producing peak positive pulses. However, this process left considerable room for further optimization, which will be addressed in Chapter 6.

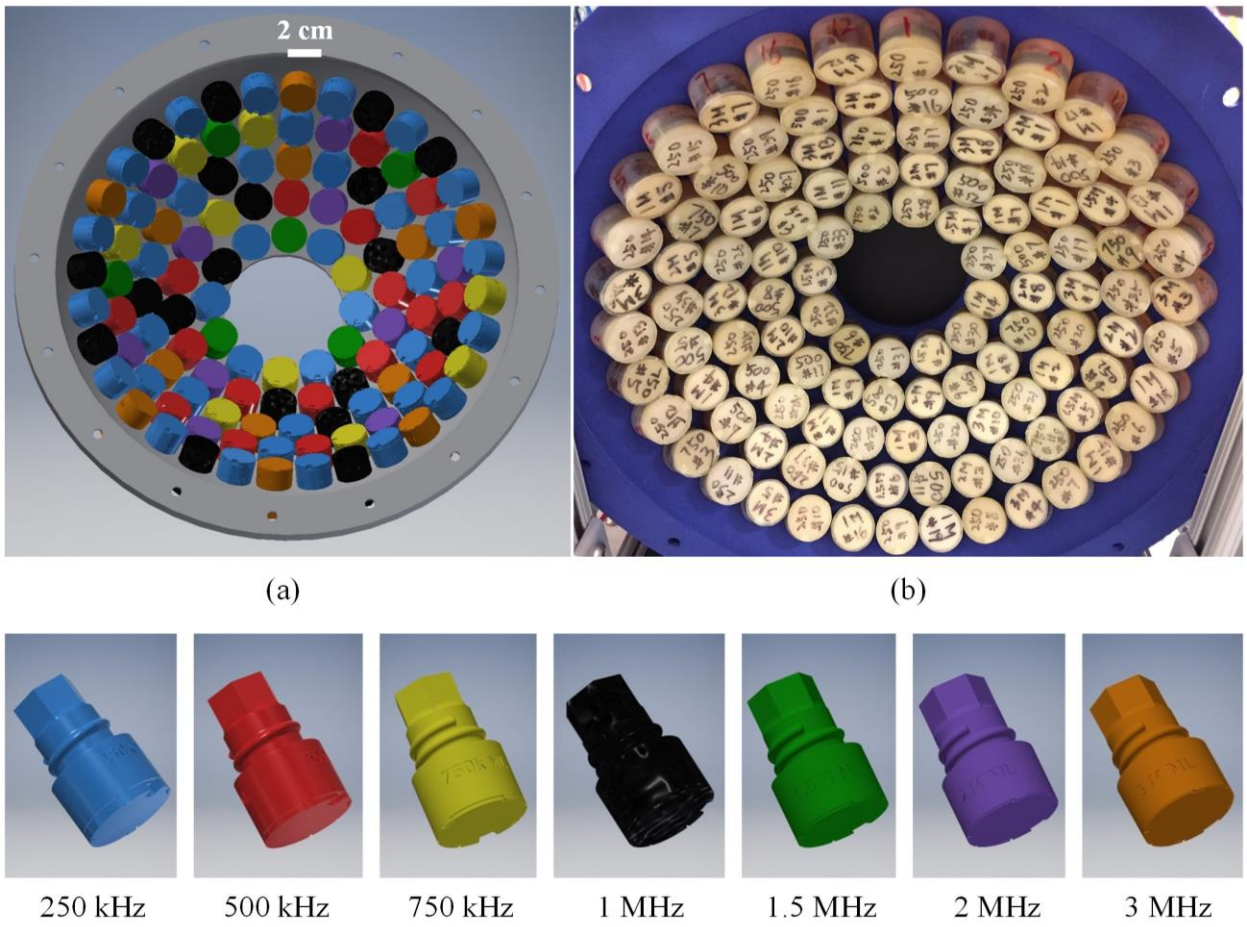

Figure 2.1 3-D design and a photograph of the frequency compounding transducer. (a) is a diagram showing the fully assembled transducer with a scaffold and individual elements color-coded for different resonant frequencies. (b) is a photograph showing the fully assembled transducer. The text on the surface of each element was used to label the resonant frequency and the number of that element.

The housings and matching layers of all individual elements were fabricated using 3-D rapid prototyping[2]. The diagram of the construction of a single element is shown in Figure 2.2. Housings for all elements were 3-D prototyped using stereolithography (SLA) with Somos 9120 material (Proto Labs, Inc., Maple Plain, MN, USA). All elements featured two matching layers. A first matching layer was bonded to the piezoelectric disc and a second matching layer was then bonded to the first matching layer, both with epoxy (LOCTITE E-00NS, Henkel). For matching layers, all elements except those in 750 kHz featured a first matching layer 3-D prototyped using

SLA with NanoTool material (Proto Labs). All elements in 750 kHz featured a first matching layer made of FR-4 sheet (G-10/FR4, McMaster-Carr, Elmhurst, IL, USA), whose material is usually used for making printed circuit boards (PCB). All elements featured a second matching layer 3-D prototyped using SLA with Somos 9120 material (Proto Labs). The acoustic impedance tests of the used materials were shown in Table 2.1. The thickness of matching layers was a quarter wavelength for optimal acoustic transmission. All elements were backed with slow-curing marine epoxy (A-side Resin 314 + B-side Slow Hardener 143, TAP Plastics, Inc., San Leandro, CA, USA).

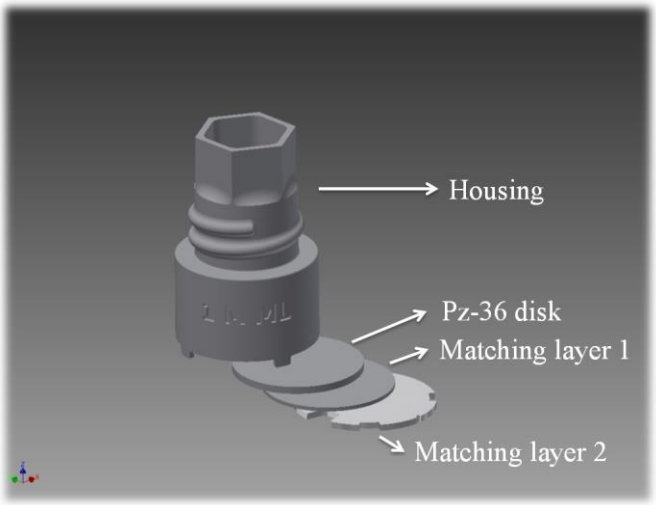

Figure 2.2 Diagram of the structure of a single element. The element consists of housing, a Pz-36 piezoelectric disk, and 2 matching layers.

Table 2.1 Impedance tests of materials used for matching layers.

Materials	Speed of sound (m/s)	Density (kg/m^3)	Impedance (MRayl)
Somos 9120	2425.2	1.16×10^3	2.81
Somos NanoTool 20L	3124.3	1.65×10^3	5.16
FR-4	3086.5	2.02×10^3	6.23

The elements were fixed on a scaffold to allow their working distance to be approximately 15 cm. The scaffold of the transducer was 3-D prototyped using selective laser sintering (SLS) with nylon material (Stratasys Direct Manufacturing, Valencia, CA, USA). After assembly, the aperture of the transducer was 25 cm. As a result, the F-number of this transducer was around 0.6.

A 256-channel high-voltage pulser system was built in-house to drive all the elements. Each individual element had two driving channels in parallel. One of them was responsible for generating short acoustic pulses with a principle peak positive pressure and the other was responsible for generating short acoustic pulses with a principle peak negative pressure. The pulser system was connected to a set of field-programmable gate arrays (FPGA) (DE0-Nano, Terasic Inc., Hsinchu, Taiwan) programmed to generate the necessary timing of outputs. The system allowed us to customize the pressure amplitudes and time delays of the short pulses generated by individual elements, which led to the generation of customizable pulsing sequences consisting of arbitrary combinations of monopolar peak positive pulses and peak negative pulses, which was not achievable with previous transducers. A fiber-optic probe hydrophone (FOPH)[3] was used to measure the ultrasound waveforms of each frequency components as well as frequency compounded pseudo-monopolar peak positive pulses and peak negative pulses at the focus of the transducer in deionized, degassed water (gas saturation below 20%). The waveforms were processed with Matlab (MathWorks, Natick, MA, USA). The gas saturation was monitored by using a portable meter (Orion Star A323 RDO/DO, Thermo Fisher Scientific, Waltham, MA, USA).

2.1.2 Results: Focal Waveforms of Pseudo-Monopolar Ultrasound Pulses

For generation of pseudo-monopolar peak positive pulses, we measured temporal focal waveforms from all individual frequency components and frequency compounded peak positive pulses. Representative waveforms are shown in Figure 2.3. All waveforms were measured directly by using the FOPH in deionized, degassed water. As shown in Figure 2.3 (a1)-(a7), for each resonant frequency, we could generate a short pulse with a principal peak positive pressure and they could be aligned temporally with correct time delays. Figure 2.3 (b) shows the pseudo-monopolar peak positive pulse. For the peak positive pulse, the peak negative pressure was 5.7 MPa and the peak positive pressure was 36.5 MPa. The peak negative pressure was from a negative phase right in front of the high-pressure positive phase.

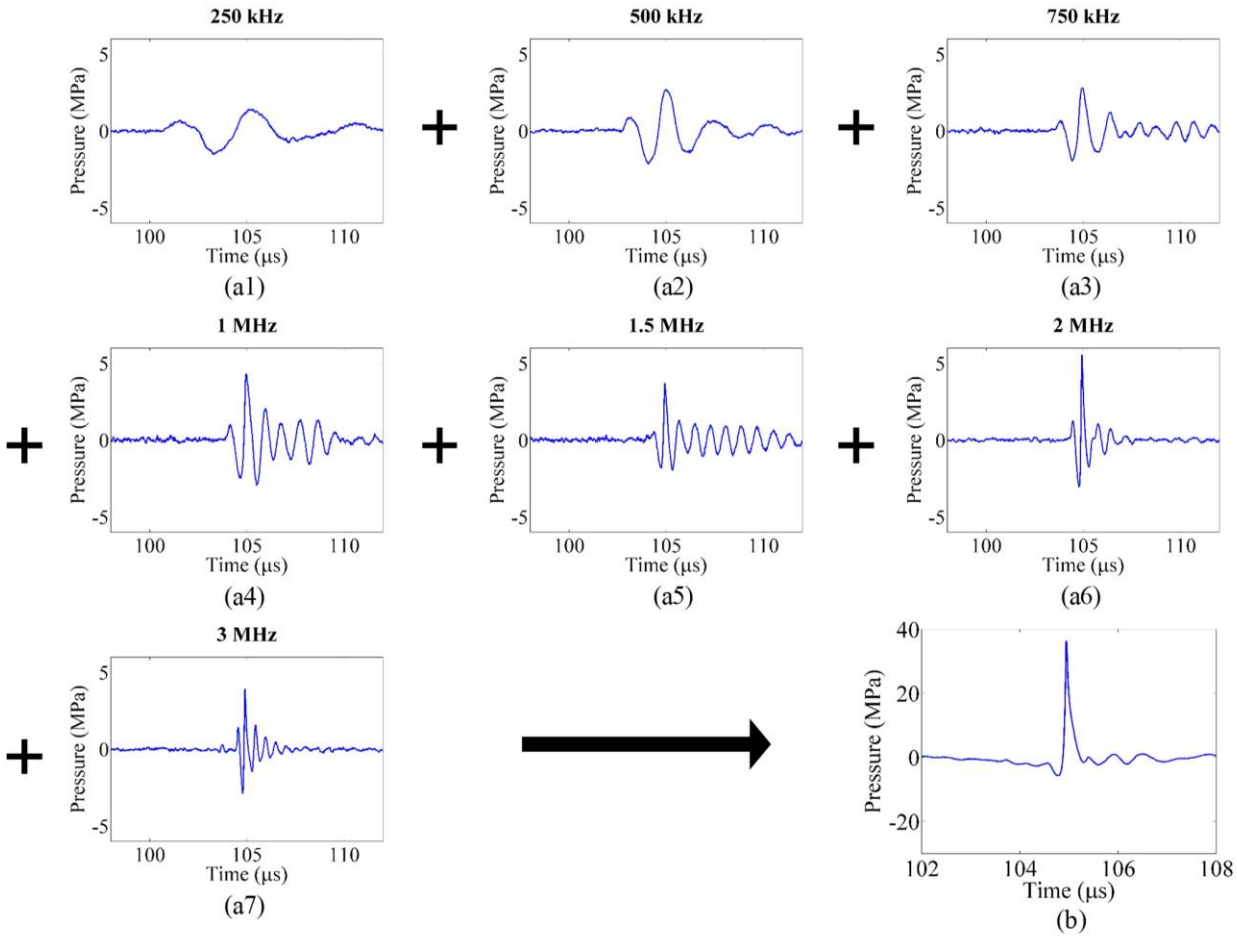

Figure 2.3 Representative temporal focal waveforms for individual frequency components and a frequency compounded pseudo-monopolar peak positive pulse. (a1)-(a7) are waveforms with a principal peak positive pressure for individual frequency components, measured in water directly by using the FOPH. (b) is the waveform for a frequency compounded pseudo-monopolar peak positive pulse, measured in water directly by using the FOPH. The peak negative pressure was 5.7 MPa and the peak positive pressure was 36.5 MPa.

For generation of pseudo-monopolar peak negative pulses, we measured temporal focal waveforms from all individual frequency components and frequency compounded peak negative pulses. Representative waveforms are shown Figure 2.4. Again, all waveforms were measured directly by using the FOPH in deionized, degassed water. As shown in Figure 2.4 (a1)-(a7), for each resonant frequency, we could generate a short pulse with a principal peak negative pressure by inverting the polarity of the excitation signals. They could still be aligned temporally with correct time delays. Figure 2.4 (b) shows the pseudo-monopolar peak negative pulse. For the

peak negative pulse, the peak negative pressure was 9.7 MPa and the peak positive pressure was 3.0 MPa. The temporal full width at half maximum (FWHM) of the peak negative pulse was 0.30 μs. It was between the FWHMs of the principal peak negative pressures of the 1.5 MHz (0.25 μs) and 1 MHz (0.35 μs) components.

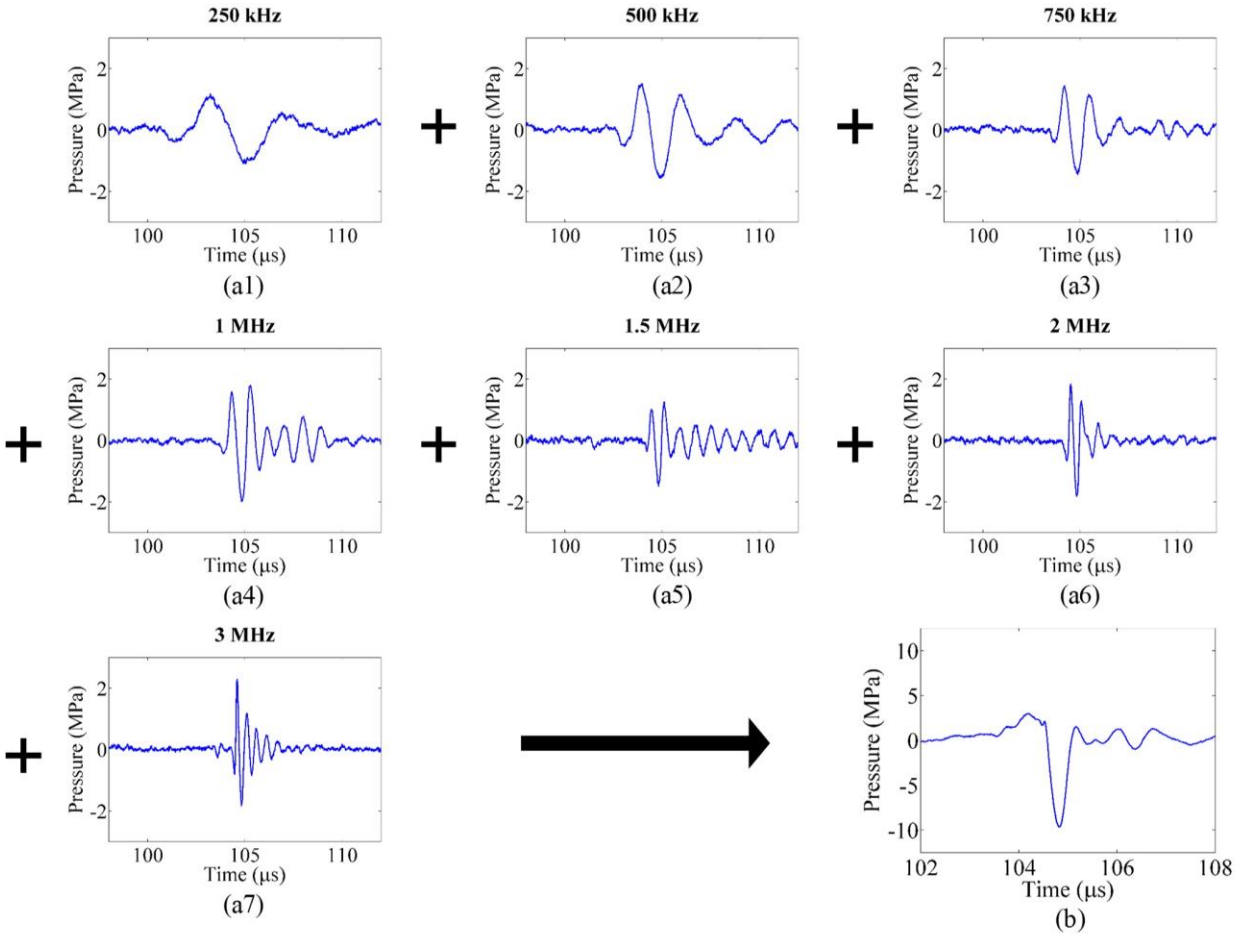

Figure 2.4 Representative temporal focal waveforms for individual frequency components and a frequency compounded pseudo-monopolar peak negative pulse. (a1)-(a7) are waveforms with a principal peak negative pressure for individual frequency components, measured in water directly by using the FOPH. (b) is the waveform for a frequency compounded pseudo-monopolar peak negative pulse, measured in water directly by using the FOPH. The peak negative pressure was 9.7 MPa and the peak positive pressure was 3.0 MPa.

2.2 References

1. Lin KW, Hall T, McGough R, Xu Z, Cain C. Synthesis of monopolar ultrasound pulses for therapy: The frequency-compounding transducer. IEEE transactions on ultrasonics, ferroelectrics, and frequency control. 2014 Jul;61(7):1123-36.

2. Kim Y, Maxwell AD, Hall TL, Xu Z, Lin KW, Cain CA. Rapid prototyping fabrication of focused ultrasound transducers. IEEE transactions on ultrasonics, ferroelectrics, and frequency control. 2014 Sep;61(9):1559-74.

3. Parsons JE, Cain CA, Fowlkes JB. Cost-effective assembly of a basic fiber-optic hydrophone for measurement of high-amplitude therapeutic ultrasound fields. The Journal of the Acoustical Society of America. 2006 Mar;119(3):1432-40.

Chapter 3 Enhanced Shock Scattering Histotripsy with Pseudo-Monopolar Ultrasound Pulses

For a multicycle shock scattering histotripsy pulse, the shock fronts are normally separated by a very short time (the period of the fundamental frequency), nominally around 1 μs[1]. As a result, the bubble cloud generated in front of the next incoming shock wave does not have enough time to evolve to a fully-grown cloud. Also, the reflected shock waves will have to interfere with the following negative pressure phases within the pulse for shock scattering to happen, which adds complexity to studying the process. Therefore, the shock scattering process might not be optimal. These factors limit the precision of shock scattering histotripsy and our ability to thoroughly study the shock scattering mechanism. To overcome those limitations, we generated independent pseudo-monopolar peak positive pulses and pseudo-monopolar peak negative pulses with variable, controllable delays, i.e., we temporally and spatially decoupled the negative and positive half-cycles in the shock scattering process.

To study the shock scattering mechanism more precisely, we initiated a primary bubble cloud ("seed cloud") at the focus by applying a single pseudo-monopolar peak negative pulse whose peak negative pressure exceeds the intrinsic threshold in the focal zone. A pseudo-monopolar peak positive pulse then arrives at the approximate peak for the expansion curve of the "seed cloud" where it is pressure-release "scattered" producing a high negative pressure phase counter-propagating with respect to the original positive monopolar pulse. A dense therapeutically effective shock scattering bubble cloud is generated when this counter-propagating negative pressure exceeds the intrinsic threshold. Since every secondary shock

scattering bubble cloud can provide a pressure-release interface for another pulse, we also proposed to generate a series of shock scattering bubble clouds (a pearl chain) by using multiple subsequent peak positive pulses after a single initial peak negative pulse. We hypothesize that these shock scattering bubble clouds can cause more precise controllable lysis when compared to more chaotic standard shock scattering histotripsy, particularly since the spatial and temporal relationship between successive pulses can now be precisely controlled.

3.1 Observations of Cavitation Bubble Clouds Generated by Enhanced Shock Scattering Histotripsy

3.1.1 Methods: Various Pulsing Sequences and High-Speed Photography

We performed experiments for observation of cavitation generated in different scenarios, so we could better understand various shock scattering phenomena in different settings. A diagram of the experiment setup is shown in Figure 3.1. The transducer was submerged in a water tank filled with deionized, degassed water (gas saturation below 20%). Cavitation was generated around the focal zone. A high-speed camera (Phantom v210, Vision Research Inc., Wayne, NJ, USA) with a focusing lens (AT-X M100 AF PRO D, Tokina, Tokyo, Japan) was used to take high-speed photography of the cavitation generated during various experiments. The field of view of the photographs was in the axial-elevational plane. The camera featured a 1280×800 CMOS sensor and the active pixel size was 20 μm. The FPGA sent trigger signals to both the high-voltage pulser and the high-speed camera so that photography and cavitation activities were synchronized. A white-light LED was used for continuous, back-lit illumination. Frame rates varied with specific experiments from 53,000 frames per second (fps) to 210,000 fps, depending on the resolution required to observe certain cavitation phenomena. Raw video

files were recorded and then saved to the computer. We then selected single frames to form a set of consecutive photographs to present the results.

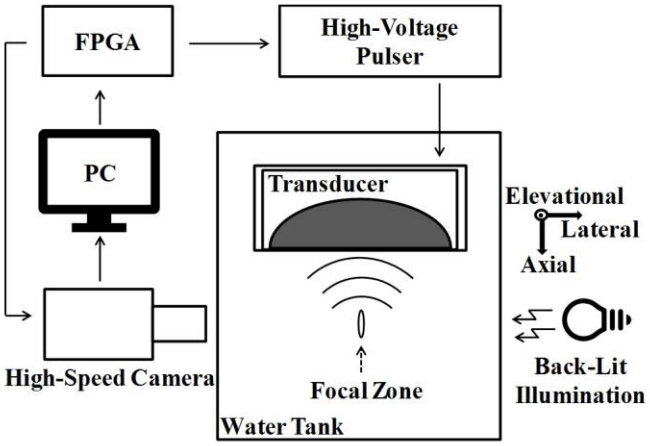

Figure 3.1 A diagram (top view) of the experiment setup for cavitation observation experiments. The frequency compounding transducer was submerged in a water tank filled with deionized, degassed water. FPGA motherboard received commands from PC and sent driving signals to a high-voltage pulser system. The high-voltage pulser then sent excitation signals to all individual elements. A high-speed camera and a back-lit illumination were used to take high-speed photography of the cavitation generated around the focal zone. The FPGA also sent trigger signals to both the high-voltage pulser and the high-speed camera so that photography and cavitation activities were synchronized. The photographs were saved to PC.

For observing the cavitation generated by enhanced shock scattering histotripsy, our first-step goal was to generate a single secondary bubble cloud by shock scattering from a primary "seed" bubble cloud and to observe the evolution completely. Thus, we started from a simple scenario where only one pseudo-monopolar peak positive pulse was applied following an initial pseudo-monopolar peak negative pulse. The time delay between the two pulses was 30 μs, which was approximately the peak time for the expansion curve of the primary bubble cloud. Similar strategy was used in studies of the effects of the time delay between shock waves in lithotripsy by Bailey et al.[2], Neisius et al.[3], Zhong et al.[4], and Handa et al.[5]. The initial peak negative pulse was applied to generate a primary bubble cloud at the focus and the following peak positive pulse was applied to generate a secondary bubble cloud by shock scattering from the primary

bubble cloud. To generate reliable cavitation, we increased the pressure levels for both the peak positive pulse and the initial peak negative pulse. The pressures applied were measured in deionized, degassed water (gas saturation below 20%) by using the FOPH. They remained unchanged for later experiments, including the red-blood-cell (RBC) phantom results. The pulse repetition frequency (PRF) was set to 1 Hz for all experiments to eliminate memory effects[6]. The frame rate used for photography was 210,000 fps. The exposure time for a single frame was 2 μs for all experiments.

To study the shock scattering mechanism within the context of spatial limitations, we examined the number of secondary bubble clouds we could generate by applying consecutive peak positive pulses without moving the focus by phasing. Therefore, we performed an experiment where multiple peak positive pulses were applied following an initial peak negative pulse. In this case, all peak positive pulses applied following the peak negative pulse were all focusing at the same geometric focus. For this experiment, 3 peak positive pulses were applied following an initial peak negative pulse. The time delay between the initial peak negative pulse and the first peak positive pulse was 30 μs. Then, 40 μs time delay, which was approximately the peak time for the expansion curve of the secondary bubble cloud, was applied between adjacent peak positive pulses. The frame rate used for photography was 140,000 fps.

After studying the case without phasing, we investigated the focus moving case, where we wanted to generate a series of consecutive secondary bubble clouds with the focus moving towards the transducer. We phased the peak positive pulses step-by-step axially towards the transducer. With this pulsing strategy we can achieve enhanced shock scattering histotripsy using almost all positive pressure shock fronts, the advantage of which will be discussed later.

To achieve step-by-step phasing, the first peak positive pulse arrived at the geometric focus. Then, the second peak positive pulse arrived at a point that was 0.9 mm closer to the transducer in the axial direction. The step was chosen based on the approximate maximum diameter of a single secondary bubble cloud. Each succeeding pulse arrived 0.9 mm closer to the transducer. For these experiments, 18 peak positive pulses were applied following an initial peak negative pulse. The time delay between the initial peak negative pulse and the first peak positive pulse was 30 μs. Then, 40 μs time delay was applied between adjacent peak positive pulses. The frame rate used for photography was 53,000 fps.

3.1.2 Results: High-Speed Images of Cavitation Bubble Clouds with Different Pulsing Sequences

We first measured the pressure levels of the applied pseudo-monopolar peak negative pulses and pseudo-monopolar peak positive pulses. The pressure levels applied for the peak negative pulse were shown in Table 3.1. The focal pressure levels for individual frequency components were measured directly by using the FOPH. The P- pressure level for the peak negative pulse was from the linearly summed signal and it was not directly measured due to cavitation. A representative waveform of the applied peak positive pulse is shown in Figure 3.2. The waveform was measured directly by using the FOPH. For the peak positive pulse, the peak negative pressure was 18.0 MPa and the peak positive pressure was 63.4 MPa.

Table 3.1 Applied focal negative pressure levels.

250 kHz	500 kHz	750 kHz	1 MHz	1.5 MHz	2 MHz	3 MHz	Focal peak negative pressure of linearly summed signal* (MPa)
3.2	5.0	6.5	6.5	4.1	6.2	5.0	34.5
*The pressure level in this column was the peak negative pressure of the linearly summed waveform. It was not directly measured.							

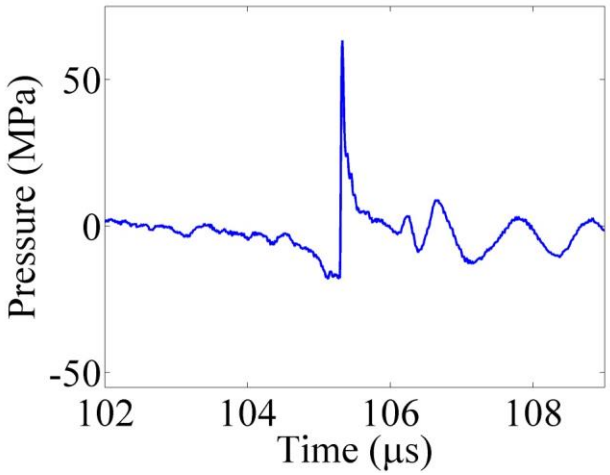

Figure 3.2 Representative temporal focal waveform for a pseudo-monopolar peak positive pulse applied. The pulse was applied in the cavitation observation experiments and RBC phantom experiments. The waveform was measured in water directly by using the FOPH. The peak negative pressure was 18.0 MPa and the peak positive pressure was 63.4 MPa.

The cavitation generated by one peak positive pulse following an initial peak negative pulse is shown in Figure 3.3. The transducer was on the left side of the field of view, so the ultrasound was propagating from left to right. The orientation was the same for later results. At 0 μs, several small bubbles were generated at the focus by the peak negative pulse because its peak negative pressure exceeded the intrinsic threshold. The bubbles then coalesced into a primary bubble cloud. A white cross marks the approximate center location of those small bubbles to indicate their initiation location so that potential movement of the bubble cloud could be

monitored, although quantitative analysis of the movement was not within the scope of this study. The cross remained at its original location throughout all frames. At 30 μs, the peak positive pulse arrived at the focus and impinged on the primary bubble cloud. A resultant, secondary bubble cloud was generated by shock scattering. The initiation of the secondary bubble cloud was captured by the frame at 28.57 μs because the exposure time of each frame was 2 μs and the exposure covered the time point of the initiation. Right after its initiation, the dimension of the secondary bubble cloud in the elevational direction was larger than that in the axial direction. Then, the secondary bubble cloud expanded. It became almost round-shaped before collapsing and fragmenting into smaller residual bubbles. A second white cross marks the approximate initiation location of the secondary bubble cloud starting from the frame at 28.57 μs. Hence, there was only one white cross in each frame for the first three frames and there were two white crosses for the rest of the frames. We observed that the primary bubble cloud moved slightly away from the transducer and the secondary bubble cloud didn’t move significantly throughout its lifespan.

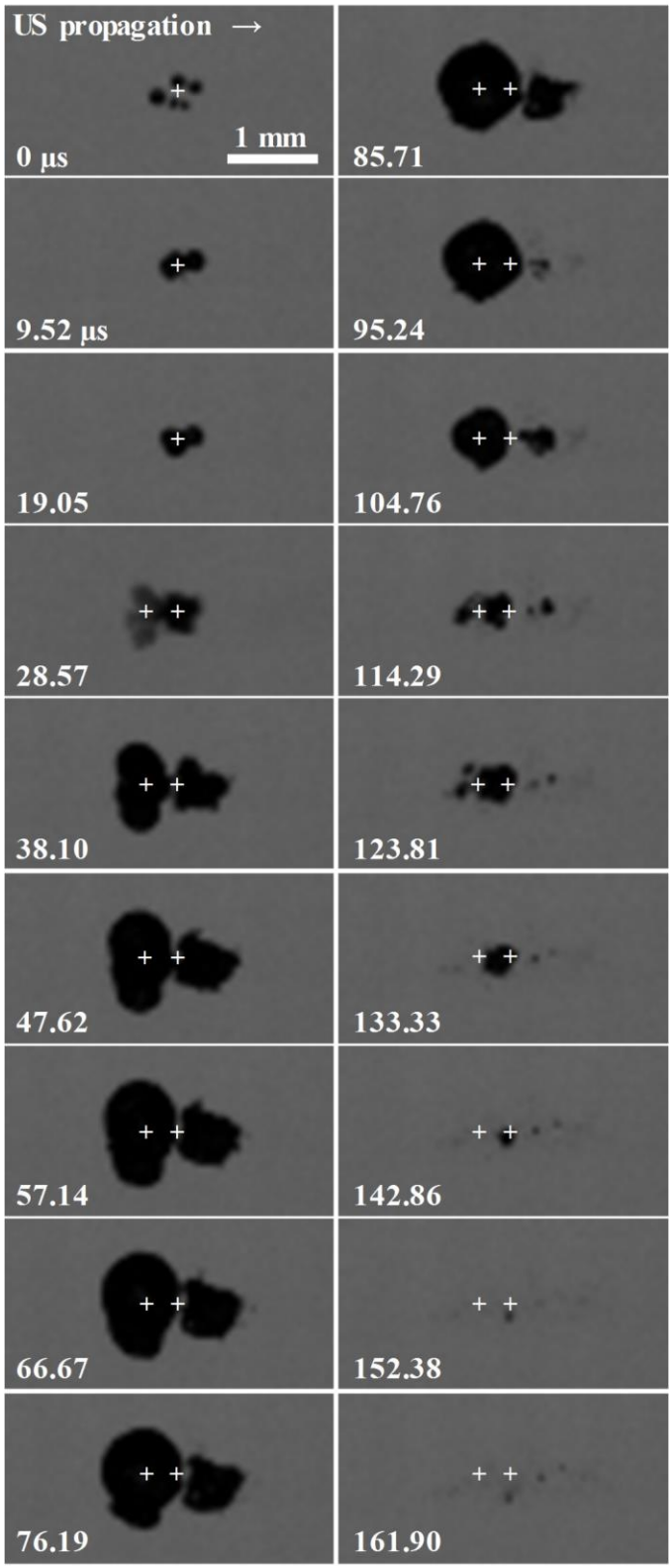

Figure 3.3 High-speed photography of the cavitation generated by a peak positive pulse following an initial peak negative pulse. The time delay between two pulses was 30 µs.

Ultrasound was propagating from left to right. At 0 μs, several small bubbles marked with a white cross were generated at the focus by the peak negative pulse because its peak negative pressure exceeded the intrinsic threshold. From the frame at 28.57 μs, a secondary bubble cloud marked with a second white cross was generated by shock scattering and observed (the exposure time was 2 μs for each frame). The secondary bubble cloud expanded after being generated. It became almost round-shaped before collapsing. The white crosses indicated the initiation locations of the bubble clouds and remained at their original locations through all frames to provide a reference for observing potential bubble movement.

The cavitation generated by multiple peak positive pulses following an initial peak negative pulse without phasing is shown in Figure 3.4. At 0 μs, a small bubble was generated by the initial peak negative pulse. A white cross marks its approximate initiation location. Starting from the frame at 28.57 μs, we could observe a first secondary bubble cloud marked with a second white cross. The bubble cloud expanded and gradually reached its maximum size before the next peak positive pulse arrived. Starting from the frame at 71.43 μs, a second secondary bubble cloud marked with a third white cross was observed. In the frames of 71.43 μs to 100.00 μs, we could observe that the primary bubble cloud and the first secondary bubble cloud coalesced into a complex shape and they seemed to be migrating away from the transducer. Finally, starting from the frame at 114.29 μs, we could observe a third secondary bubble cloud marked with a fourth white cross. Overall, 3 secondary bubble clouds were generated by 3 peak positive pulses. After around 3 secondary bubble clouds, the process could no longer generate shock scattering bubble clouds because the peak positive pressure around the front edge of the third secondary cloud was not sufficient due to movement of the clouds away from the focus.

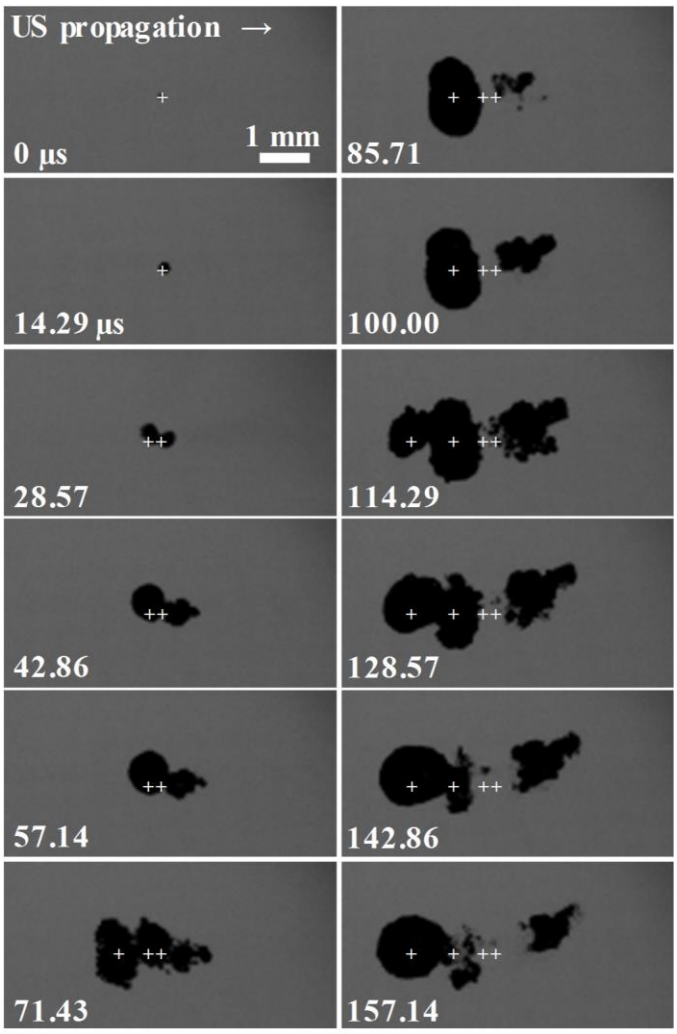

Figure 3.4 High-speed photography of the cavitation generated by multiple peak positive pulses without phasing. All 3 peak positive pulses applied were focusing at the geometric focus. The time delay between the peak negative pulse and the first peak positive pulse was 30 µs. Then, 40 µs time delay was applied between adjacent peak positive pulses. A primary bubble cloud marked with a white cross was generated at 0 µs. From the frame at 28.57 µs, a first secondary bubble marked with a second white cross could be observed. From the frame at 71.43 µs, a second secondary bubble marked with a third white cross could be observed. From the frame at 114.29 µs, a third secondary bubble marked with a fourth white cross could be observed.

The cavitation generated by multiple peak positive pulses following an initial peak negative pulse with step-by-step phasing is shown in Figure 3.5. 16 secondary bubble clouds were generated in total by 16 peak positive pulses phasing gradually towards the transducer. At 0 µs, several small primary bubbles marked with a white cross were generated. At 37.7 µs, a first secondary bubble cloud marked with a white arrow was observed. At 75.5 µs, a second

secondary bubble cloud was observed. At 188.7 µs, the initiation of the 5th secondary bubble cloud was barely visible because for that frame, the 2-µs exposure time of the camera barely covered the initiation of the bubble cloud. However, at 226.4 µs, we could observe the 5th secondary bubble cloud clearly because the bubble cloud had been initiated and evolved. As time progressed, at 641.5 µs, a 16th secondary bubble cloud was observed. Overall, we could see that with each peak positive pulse, a new secondary bubble cloud was generated by shock scattering. The bubble clouds kept growing towards the transducer and the overall resultant cloud had an elongated shape. We found out that after the 16th peak positive pulse, there was no more shock scattering cavitation because the peak positive pulse was out of the steering range of the transducer and we did not include those frames due to limited space.

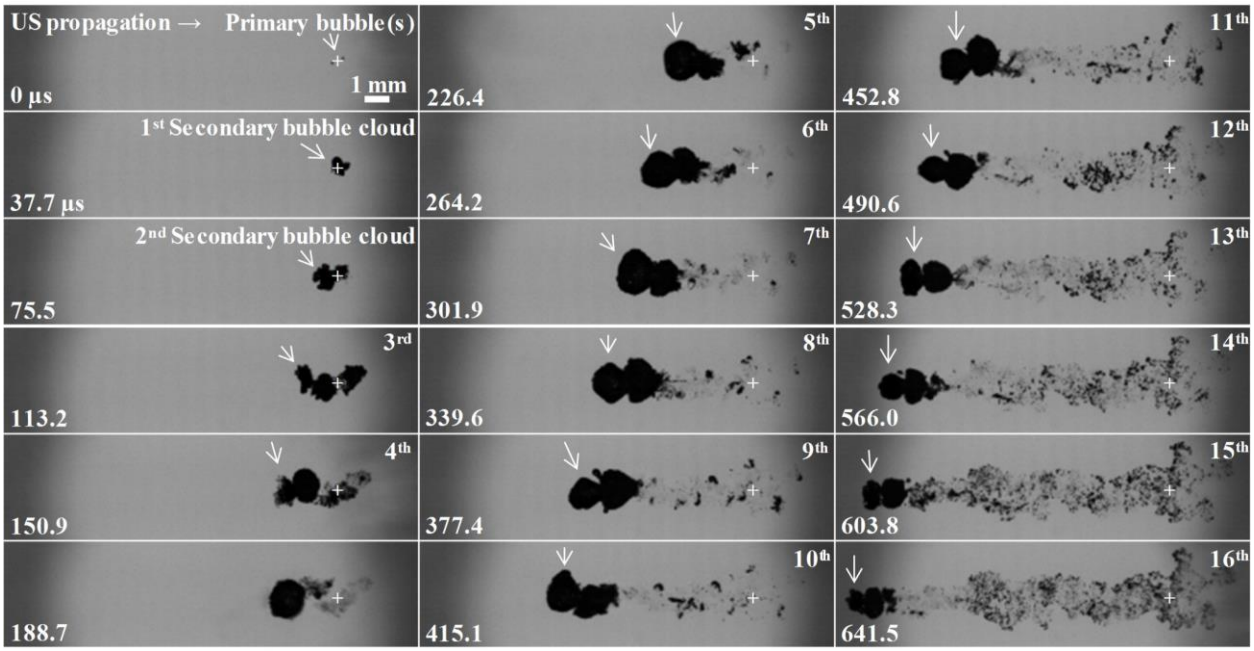

Figure 3.5 High-speed photography of the cavitation generated by multiple peak positive pulses with phasing. A step was uniformly 0.9 mm towards the transducer in the axial direction. The time delay between the peak negative pulse and the first peak positive pulse was 30 µs. Then, 40 µs time delay was applied between adjacent peak positive pulses. 16 secondary bubble clouds were generated in total and the overall bubble cloud kept growing towards the transducer, resulting in an elongated shape. A white cross marked the initiation location of the primary bubble cloud. Each secondary bubble cloud was marked with a white arrow. The shadows on the left and right side of each frame were areas outside of the boundary of the back-lit illumination.

3.2 Therapeutic Feasibility Test with Red-Blood-Cell Phantoms

3.2.1 Methods: Making Red-Blood-Cell Phantoms

RBC tissue-mimicking phantoms were used to test the therapeutic feasibility of enhanced shock scattering histotripsy. RBC phantoms were used to visualize damage induced by cavitation[7]. We made RBC phantoms based on the methods described in previous studies[7, 8]. The agarose-saline mixture was made of low-EEO/multipurpose agarose powder (BP160-500, Fisher Scientific, Hampton, NH, USA) and degassed phosphate buffer saline. The ratio of the mixture was 1:100 (w:v). The central layer of the phantom that contained RBCs was made to be around 500 μm to 600 μm in thickness. The ratio of RBCs to agarose-saline mixture was 6:44 (v:v) to obtain a sufficient contrast between undamaged and damaged regions. During the experiments, the phantom was held by a gel holder and the gel holder was firmly attached to a 3-axis stepper motor positioning system for mobility. Two axes of the system featured 17MDSI stepper motors (Anaheim Automation, Anaheim, CA, USA) and one axis featured a 23MDSI stepper motor (Anaheim). The gel holder was positioned such that the central layer of the phantom was aligned with the axial direction of the transducer and the layer overlapped with the focal zone. The alignment was confirmed by successfully generating a sample lesion at the beginning of the experiments.

To generate a lesion in an RBC phantom using enhanced shock scattering histotripsy, 16 peak positive pulses with step-by-step phasing were applied after an initial peak negative pulse. The time delay between the initial peak negative pulse and the first peak positive pulse was 30 μs. Then, 40 μs time delay was applied between adjacent peak positive pulses. Up to 400 repetitions of those pulses were applied. The PRF was set to 1 Hz. 16 peak positive pulses were chosen based on results from the cavitation observation experiments with phasing. Photographs

were taken after 10, 100, 200, 400 repetitions were applied to observe the progression of the lesion. A reference photograph was also taken under the pre-treatment condition.

3.2.2 Results: Lesion Generated in Red-Blood-Cell Phantoms

The lesion generated by enhanced shock scattering histotripsy is shown in Figure 3.6. Prior to the first burst (pre-treatment), the field of view was dark because the RBC layer blocked the back-lit illumination. After 10 repetitions, we could start to observe RBC lysis introduced by cavitation, especially around the geometric focus. The damage was seen in bright spots since illumination could then reach the camera. The last phasing position was also marked manually in the photographs to refer to the point where the last peak positive pulse was focusing. After 400 repetitions, we could observe an elongated, "cigar-shaped" lesion. The boundary between damaged and undamaged regions was clear and there was no significant damage outside of the lesion.

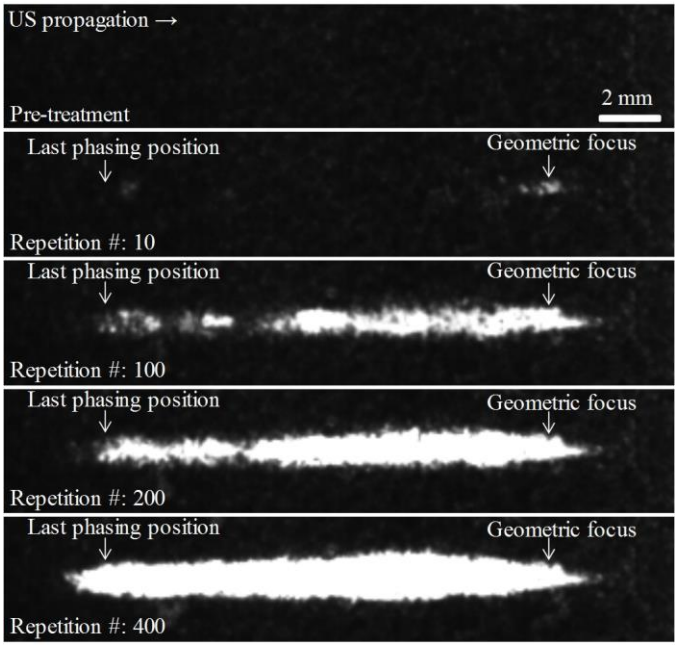

Figure 3.6 Representative photographs of a lesion generated in an RBC phantom. Photographs were taken after 10, 100, 200, 400 repetitions of enhanced shock scattering histotripsy pulses. A reference photograph was also taken under the pre-treatment condition. The field of view was

dark because the RBC layer blocked the back-lit illumination. After 10 repetitions, damage induced by cavitation could be observed, especially around the geometric focus. The geometric focus and the last phasing position were both marked with a white arrow. After 400 repetitions, an elongated lesion could be observed.

3.3 Pre-Focal Cavitation at Tissue Interfaces

Cavitation bubble clouds generated by shock scattering histotripsy at a tissue-water interface were observed[9]. To help discuss pre-focal cavitation issues with monopolar acoustic pulses, we obtained a piece of fresh pig skin tissue from an unrelated study and observed the cavitation at the water-tissue interface when multiple peak negative pulses and peak positive pulses were applied, respectively.

3.3.1 Methods: Fresh Pig Skin Tissue and Pulses Applied

The dimensions of the tissue cut were 4 cm in width, 8 cm in height, and 3 mm in thickness (Figure 3.7). It was positioned 1.5 cm closer to the transducer in the axial direction with respect to the focus. The interior layer of the pig skin was facing the transducer to provide a pre-focal, water-tissue interface for incident ultrasound pulses. The experiments were conducted within the same day of the harvest of the tissue. For peak negative pulses, the focal peak negative pressure was 44.7 MPa. 100 pulses were applied at 100 Hz PRF. For peak positive pulses, the focal peak positive pressure was 45.7 MPa, which was kept at the same pressure level as the peak negative pulses. 100 pulses were applied at 100 Hz PRF. A high-speed camera was used to observe potential cavitation activities.

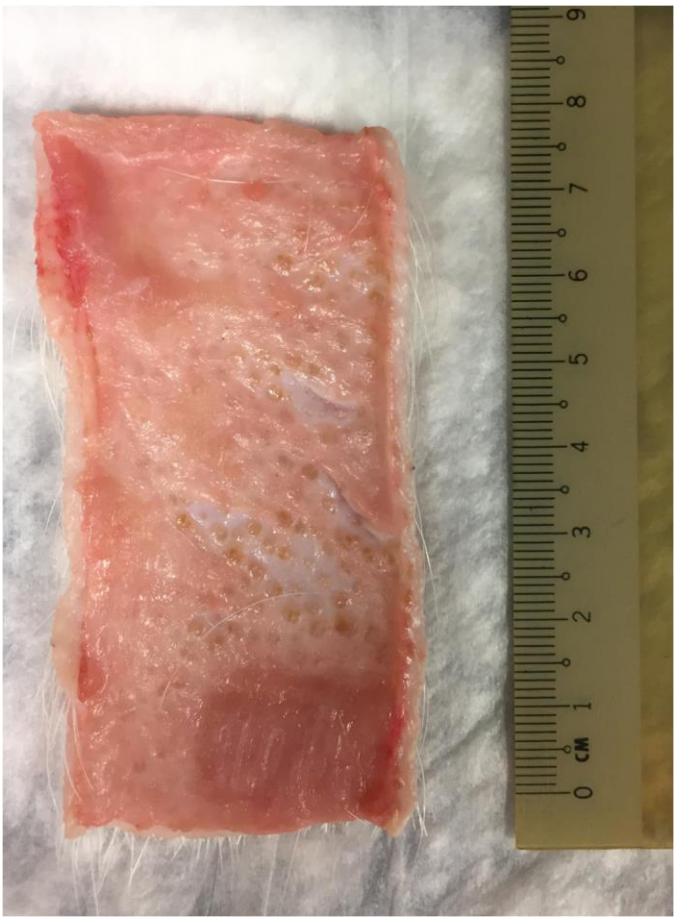

Figure 3.7 Picture of a piece of fresh pig skin tissue. During experiments, the tissue was positioned so that the interior layer (shown in the figure) was facing the transducer, creating a pre-focal, water-tissue interface for incident ultrasound waves.

3.3.2 Results: Observation of Cavitation Generated at the Tissue Interface

The representative photographs of the water-tissue interface are shown in Figure 3.8. (a) shows a representative photograph of the water-tissue interface when a P+ pulse was applied. No cavitation bubble was observed. (b) and (c) are two representative photographs when a P- pulse was applied. Cavitation bubbles were observed in both frames, which are pointed out by a white arrow. Quantitatively, we found out that for P- pulses, the cavitation did not appear until several pulses were applied. From the three experiments we performed, the average number of P- pulses needed for cavitation to become observable was 5. Also, after the appearance of the first cavitation bubbles, the average percentage of P- pulses that generated cavitation bubbles at the

interface was 85.9%. For P+ pulses, there were 0% of pulses that generated observable cavitation bubbles.

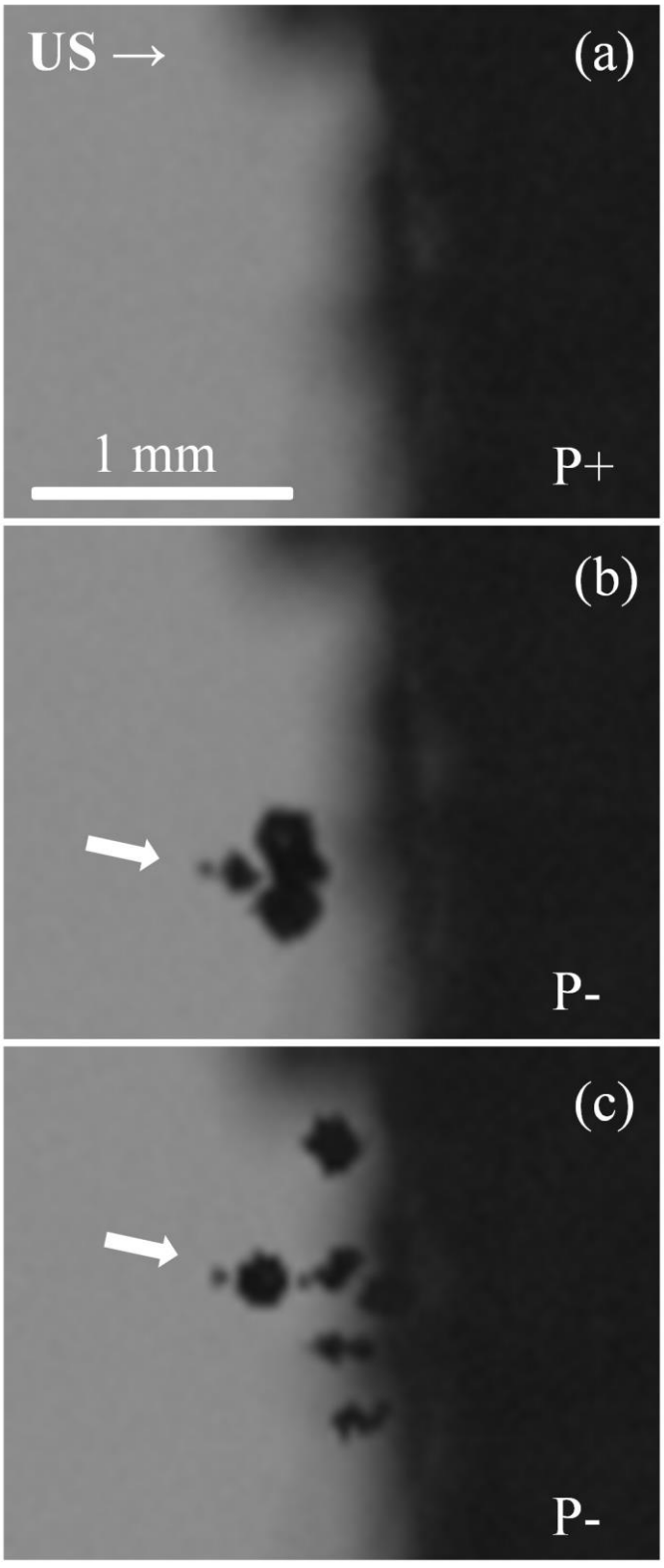

Figure 3.8 Representative photographs of the water-tissue interface when peak negative (P-) pulses and peak positive (P+) pulses were applied. The grey area is water and the dark area is the interior layer of the pig skin. (a) shows a representative photograph of the water-tissue interface

when a P+ pulse was applied. No cavitation bubble was observed. (b) and (c) are two representative photographs when a P- pulse was applied. Cavitation bubbles were observed in both frames, which are pointed out by a white arrow.

3.4 Investigation of Nonlinearity Based on Two Distributions of Individual Elements within the Transducer

For ultrasound, nonlinearity exists during the propagation of high-pressure ultrasound waves. Change of the local speed of sound leads to the introduction of extra frequency components into the original waveforms. As a result, nonlinear ultrasound waves usually become distorted.

Nonlinear propagation can be affected by various parameters of an ultrasound transducer, including F-number, pressure amplitudes, resonant frequency, etc. In previous experiments described in this chapter, we distributed all the individual elements with different resonant frequencies in a "scattered" manner, meaning all the elements at the same frequency were located as far as possible from each other. We assumed this distribution would suppress nonlinear propagation since if put together, elements at the same frequency would generate waves that would interfere constructively along propagation.

One of the advantages of how we construct the frequency compounding transducer is we can easily replace any individual element and re-distribute all of them. To investigate the effects of distribution of individual elements on nonlinearity, we distributed all the individual elements in a "grouped" manner, meaning all the elements at the same frequency were located together, or as a sub-group within the array. Then, with the same driving levels, focal waveforms of pseudo-monopolar peak positive pulses and peak negative pulses were measured from both distributions. The peak pressure amplitudes and the overall shape of the waveforms were then compared to examine potential nonlinearity differences.

3.4.1 Methods: Scattered Distribution and Grouped Distribution

3-D design of the grouped distribution is shown in Figure 3.9. Compared to the scattered distribution, which is shown in Figure 2.1, there are seven sub-aperture transducers (from seven resonant frequencies) within the overall transducer.

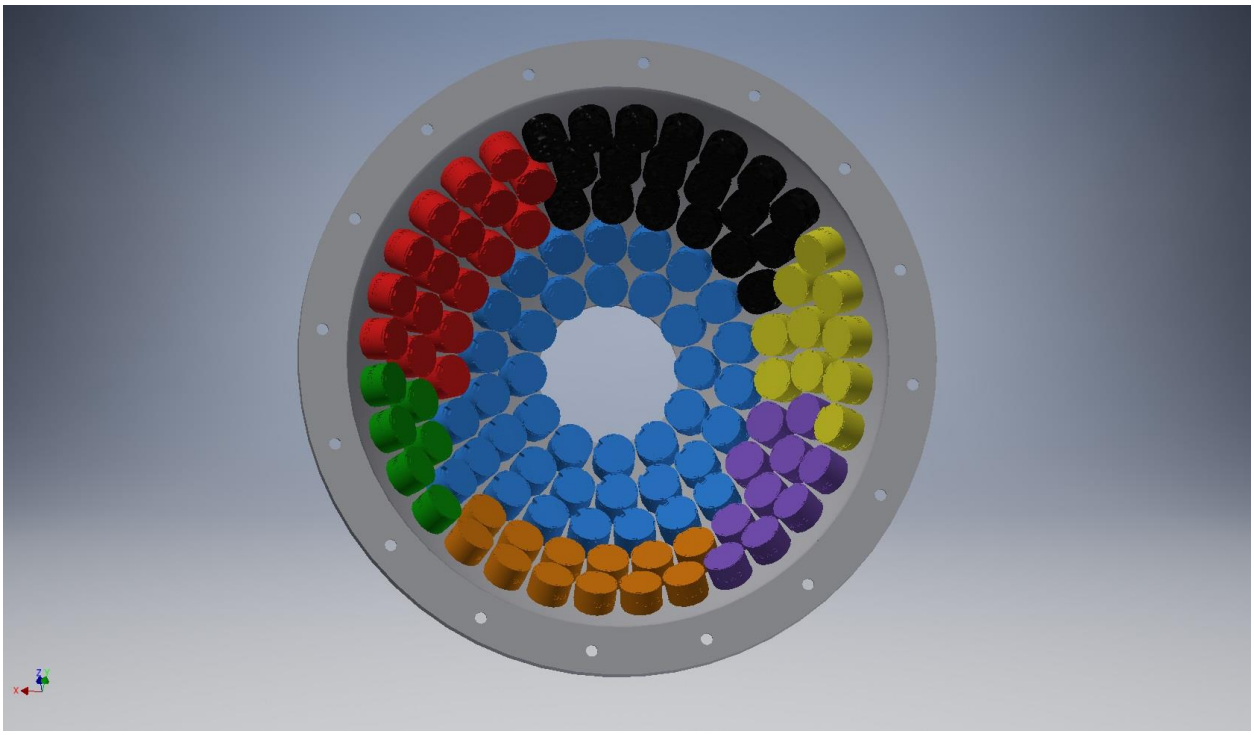

Figure 3.9 3-D design of the grouped distribution. All the elements at the same resonant frequency were intentionally put together, creating seven sub-aperture arrays within the overall transducer.

Focal waveforms of pseudo-monopolar peak positive pulses and peak negative pulses were measured by using a FOPH. Different driving levels were applied to allow a range of pressures to be compared.

3.4.2 Results: Measured Focal Waveforms and Corresponding Pressure Levels

Measured focal waveforms of pseudo-monopolar peak positive pulses with 5 different driving levels are shown in Figure 3.10. For all 4 driving levels with two waveforms successfully measured, most part of the waveforms was identical except that there were more variations after

the high-amplitude positive phase in the waveforms from the grouped distribution. As a result, the quality of the waveforms from the grouped distribution was not as good as that from the scattered distribution. Peak pressure levels, both positive and negative, with different driving levels are plotted in Figure 3.11. From the plot we can see the positive pressure levels and negative pressure levels are identical between the two distributions, indicating that the nonlinearity was not different.

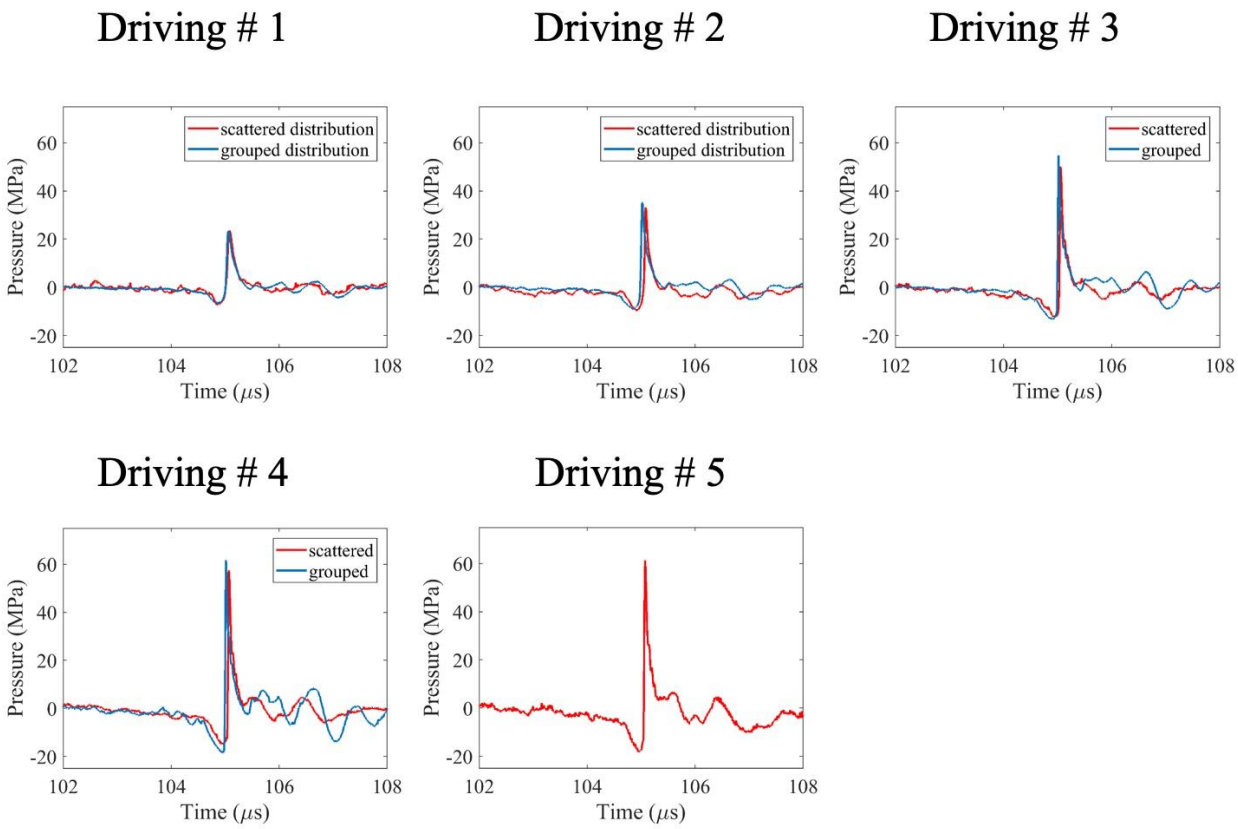

Figure 3.10 Representative focal waveforms of pseudo-monopolar peak positive pulses at 5 driving levels. Blue waveforms are from the grouped distribution and red waveforms are from the scattered distribution. 5 driving levels were applied. There was no waveform from the grouped distribution at driving level 5 due to consistent cavitation damage on the fiber of the FOPH from the high-pressure negative phase.

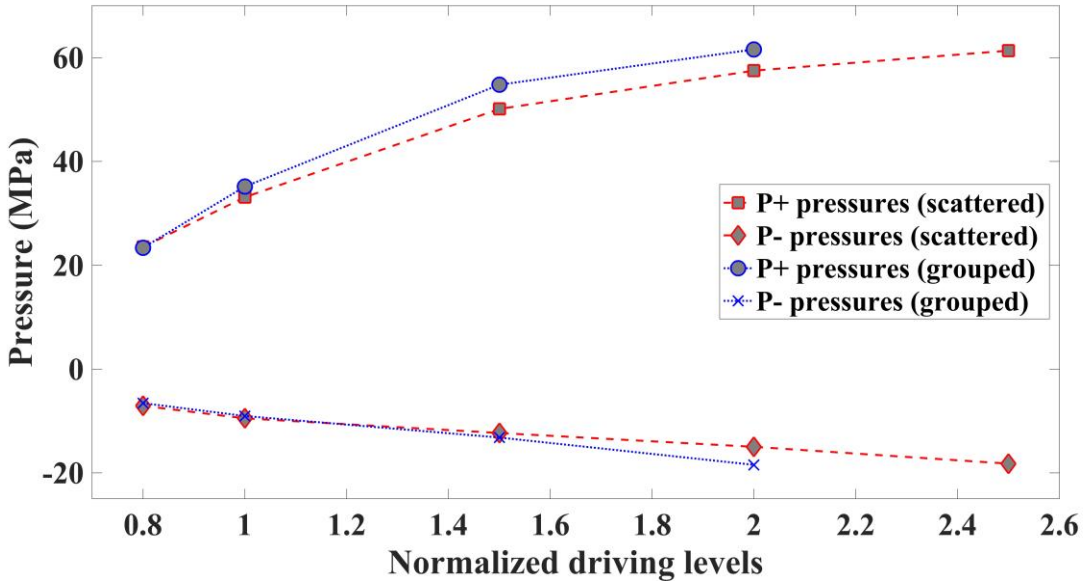

Figure 3.11 Plot of peak positive pressures and peak negative pressures with normalized driving levels from pseudo-monopolar peak positive pulses. Blue lines are from the grouped distribution and red lines are from the scattered distribution.

Measured focal waveforms of pseudo-monopolar peak negative pulses with 5 different driving levels are shown in Figure 3.12. The quality of the waveforms from the grouped distribution was not as good as that from the scattered distribution due to the big variations after the dominant negative phase. Peak pressure levels, both positive and negative, at different driving levels are plotted in Figure 3.13. The grouped distribution would give a higher peak negative pressure while the peak positive pressure was almost the same.

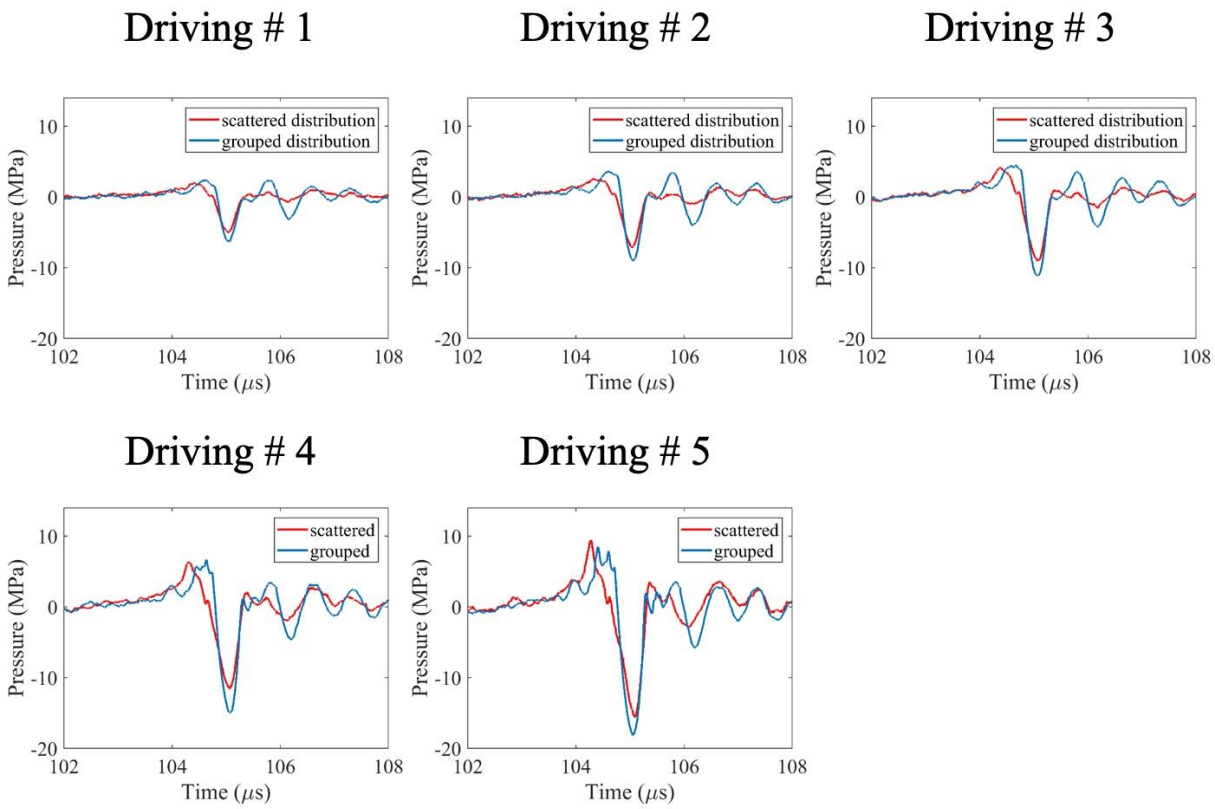

Figure 3.12 Representative focal waveforms of pseudo-monopolar peak negative pulses at 5 driving levels. Blue waveforms are from the grouped distribution and red waveforms are from the scattered distribution.

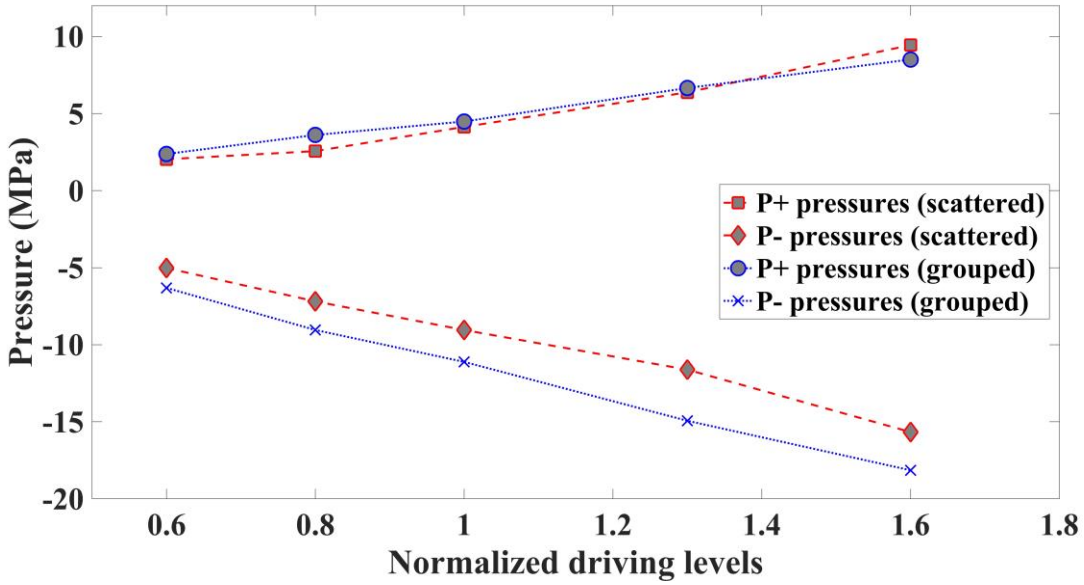

Figure 3.13 Plot of peak positive pressures and peak negative pressures with normalized driving levels from pseudo-monopolar peak negative pulses. Blue lines are from the grouped distribution and red lines are from the scattered distribution.

3.5 Discussion

There are two approaches, or methods, for doing short pulse (less than 20 cycles) histotripsy. These we have called “intrinsic threshold histotripsy” and “shock scattering histotripsy”. Intrinsic threshold histotripsy is the method that depends on creating focal waveforms part of which exceeds the intrinsic threshold (around 28 MPa negative). A very dense energetic bubble cloud can then be generated with very nearly 100% probability. For shock scattering histotripsy, the negative pressures of the focal waveform usually do not directly exceed the intrinsic threshold. These lower negative pressures create sparse populations of incidental bubbles which do not effectively mechanically fractionate tissue. However, therapeutically effective bubble clouds are still generated in this method from the interaction of the shock waves with incidental bubbles and the negative phases within the pulses, which is addressed in detail earlier in the chapter.

Intrinsic threshold histotripsy is by far the most effective and versatile method of creating dense therapeutically effective bubble clouds wherein at least one negative half-cycle of the focal waveform exceeds directly the intrinsic threshold. However, when the target volume is deep and occluded by gas bodies and/or bone, it is often impossible to directly exceed the intrinsic threshold. Fortunately, if the maximum peak negative focal pressure exceeds about 20 MPa (sometimes a little lower, but higher than 15 MPa), it is possible to generate energetic bubble clouds by shock scattering histotripsy. In this method, nonlinear propagation can generate positive shock fronts with peak pressures many times the magnitude of negative pressures. Nonlinear shock front generation can be thought of as a natural pulse amplification process making shock scattering histotripsy possible. These high positive pressures do not harm tissue unless they are reflected or back-scattered from a pressure release (gaseous) surface. The resulting pressure inversion can easily exceed the intrinsic threshold. In shock scattering histotripsy, the pressure release scattering bodies are created at the focus by the first several negative half cycles in the form of incidental bubbles. The process is made easier when the scattered shock front, a newly generated peak negative pressure, adds coherently with the next negative phase of the counter-propagating incident histotripsy waveform. The generated histotripsy bubble clouds are often rather chaotic and not very repeatable in shape but can be quite effective in fractionating tissue.

A significant disadvantage of shock scattering histotripsy can be an unfortunate result of the many negative half cycles of the therapy pulse which is typically from 3 to 10 cycles in length. These negative half cycles are effective at generating the necessary incidental “seed” bubbles at the focus from which shock scattering occurs but can also generate many incidental bubbles pre-focally. Accumulation of these pre-focal bubbles can be treatment limiting as they

can significantly attenuate the primary histotripsy pulse. Thus, pre-focal cavitation, particularly at tissue interfaces, is a major limiting factor in treatment of target volumes at depth with standard shock scattering histotripsy.

The enhanced histotripsy method presented in this study was created partly to alleviate this problem. This approach decouples the generation of the seed cloud from the following positive shock front because they are separate independent waveforms. Moreover, using frequency compounding technology, both positive and negative pulses can be synthesized to approximate monopolar pulses wherein only a single principal negative or positive half cycle is generated. With independent temporal and spatial control of these quasi-monopolar pulses, the number of parameters that can be changed to optimize the shock scattering process becomes quite large.

For example, in the 16-pulse pearl-chain bubble cloud produced in this study, an elongated therapeutically effective set of consecutive bubble clouds were generated with each 16-cloud pearl-chain requiring only one seed cloud forming negative half cycle greatly reducing pre-focal cavitation because virtually everything is accomplished with monopolar positive pulses. Contrast this with standard shock scattering histotripsy with an 8-cycle pulse. To generate a 16-cloud pearl-chain, 8×16, or 128 negative half cycles, traverse the pre-focal zone greatly enhancing the potential for treatment limiting pre-focal cavitation. Compare this to only a single negative half cycle required for the pearl-chain formation exemplified in this study. This result is magnified if multiple repetitions of the pearl chain are required to completely homogenize the tissue.

Another disadvantage of standard shock scattering histotripsy relates to the bubble cloud emission signals that can be received at the transducer. In intrinsic threshold histotripsy, a single

negative half-cycle generates dense regular shaped bubble clouds that emit a large clean signal propagated back to the transducer due to the energetic initial expansion of the cloud[10]. These signals may be useful for aberration correction. However, the emission from standard shock scattering histotripsy clouds is rather chaotic and provides inconsistent timing information[11]. Since we use single pseudo-monopolar pulses for enhanced shock scattering histotripsy, the generated clouds are remarkably regular and repeatable in shape. The clean emission signals can provide accurate timing information for aberration correction, extremely useful from deep focal volumes wherein aberration correction can greatly increase the quality of the focal waveforms. This self-generation of accurate aberration correction "beacon" signals from the focus is an important feature of some forms of histotripsy.

Finally, it should be noted that the spatial and temporal parameters used in this study to generate the pearl-chain clouds are insensitive to even relatively large changes in both timing of the next pulse and its placement in the front of the previous pulse. We tried many variations in timing of succeeding pulses and the placement of their foci (with respect to the preceding cloud) with essentially the same interesting results.

3.6 References

1. Maxwell AD, Wang TY, Cain CA, Fowlkes JB, Sapozhnikov OA, Bailey MR, Xu Z. Cavitation clouds created by shock scattering from bubbles during histotripsy. The Journal of the Acoustical Society of America. 2011 Oct;130(4):1888-98.

2. Bailey MR. Control of acoustic cavitation with application to lithotripsy. The Journal of the Acoustical Society of America. 1997 Aug;102(2):1250-.

3. Neisius A, Smith NB, Sankin G, Kuntz NJ, Madden JF, Fovargue DE, Mitran S, Lipkin ME, Simmons WN, Preminger GM, Zhong P. Improving the lens design and performance of a contemporary electromagnetic shock wave lithotripter. Proceedings of the National Academy of Sciences. 2014 Mar 13:201319203.

4. Zhong P, Cocks FH, Cioanta I, Preminger GM. Controlled, forced collapse of cavitation bubbles for improved stone fragmentation during shock wave lithotripsy. The Journal of urology. 1997 Dec 1;158(6):2323-8.

5. Handa RK, McAteer JA, Willis LR, Pishchalnikov YA, Connors BA, Ying J, Lingeman JE, Evan AP. Dual-head lithotripsy in synchronous mode: acute effect on renal function and morphology in the pig. BJU international. 2007 May;99(5):1134-42.

6. Wang TY, Xu Z, Hall TL, Fowlkes JB, Cain CA. An efficient treatment strategy for histotripsy by removing cavitation memory. Ultrasound in medicine & biology. 2012 May 1;38(5):753-66.

7. Maxwell AD, Wang TY, Yuan L, Duryea AP, Xu Z, Cain CA. A tissue phantom for visualization and measurement of ultrasound-induced cavitation damage. Ultrasound in medicine & biology. 2010 Dec 1;36(12):2132-43.

8. Lin KW, Hall T, McGough R, Xu Z, Cain C. Synthesis of monopolar ultrasound pulses for therapy: The frequency-compounding transducer. IEEE transactions on ultrasonics, ferroelectrics, and frequency control. 2014 Jul;61(7):1123-36.

9. Xu Z, Raghavan M, Hall TL, Mycek MA, Fowlkes JB, Cain CA. Evolution of bubble clouds induced by pulsed cavitational ultrasound therapy-histotripsy. IEEE transactions on ultrasonics, ferroelectrics, and frequency control. 2008 May;55(5).

10. Macoskey JJ, Hall TL, Sukovich JR, Choi SW, Ives K, Johnsen E, Cain CA, Xu Z. Soft-Tissue Aberration Correction for Histotripsy. IEEE transactions on ultrasonics, ferroelectrics, and frequency control. 2018 Nov;65(11):2073-85.

11. Vlaisavljevich E, Maxwell A, Warnez M, Johnsen E, Cain C, Xu Z. Histotripsy-induced cavitation cloud initiation thresholds in tissues of different mechanical properties. IEEE transactions on ultrasonics, ferroelectrics, and frequency control. 2014 Feb;61(2):341-52.

Chapter 4 Cavitation Thresholds at Pressure-Release Interfaces with Pseudo-Monopolar Ultrasound Pulses

In this chapter, experiments are designed and performed to investigate the cavitation thresholds at pressure-release interfaces with pseudo-monopolar peak positive pulses, as well as the differences of the cavitation bubble clouds generated by peak negative pulses and peak positive pulses on an air pocket inclusion model. The main purpose of these studies is to provide experimental evidence and help address some of the safety issues with therapeutic ultrasound, although specific clinical applications may not be discussed. In Chapter 3, it is mentioned that one of the advantages of enhanced shock scattering histotripsy is that we can generate therapeutically effective cavitation bubble clouds by using mostly pseudo-monopolar peak positive pulses, which could reduce the probability of introducing pre-focal incidental bubbles since the application of negative pulses is minimized. It is commonly accepted that peak positive pressures are safe clinically if the mechanical index (MI) is examined since MI only takes the peak negative pressure into consideration. However, the propagation path of ultrasound waves in a clinical situation may be a complex one with multiple layers of tissues with different acoustic impedances. It could even be an approximate pressure-release interface if we look at regions around the lung. In these situations, it might be very dangerous to ignore the effects possibly brought by peak positive pressures. We propose to look at the cavitation generated by peak positive pressures at pressure-release surfaces in the propagation path. Several different water-air interface models are used to study the cavitation thresholds at pressure-release interfaces. A gas pocket model is also investigated to study the cavitation bubble clouds generated by peak

positive pulses and peak negative pulses at certain pressure levels. Clinically, this could be a model comparable to the alveolar sacs in the lung.

4.1 Pressure-Release Interfaces

The pressure-release surface in acoustics is defined as a surface where the amplitude of the reflected wave is equal to that of the incident wave, and the transmitted wave has zero pressure amplitude[1]. This phenomenon comes from the fact that the acoustic impedance of the first medium where the incident waves travel is much higher than that of the second medium where the transmitted waves exist. This results in a pressure reflection coefficient of -1. If the incident wave is a peak positive pulse, the reflected wave will then become a peak negative pulse with the same pressure amplitude. If the amplitude exceeds a certain threshold, cavitation bubble is expected to be generated.

In previous studies where the intrinsic threshold was investigated, the focal peak negative pressure was linearly summed since no hydrophone measurement was possible when cavitation was generated. However, peak positive pressures can be directly measured by using a FOPH. With a pressure-release interface, the peak positive pressure will be reflected and then becomes a negative pressure traveling back towards the transducer. With exact positive pressure measurements and the pressure-release interfaces, accurate cavitation thresholds can be characterized.

Several models are introduced to act as the pressure-release interfaces in the experiments. The first one is an acrylic packing tape (341, Intertape Polymer Group, USA) with a thickness of 3 mil (0.0762 mm). The second one is a PVC shrink film with a thickness of 75 GA (0.0190 mm). The choices of materials considered thickness, rigidity, and commercial availability. The thickness is expected to be as thin as possible. At the same time, the material needs to have

certain rigidity because potential movements of the material due to radiation force should be minimized. The third material is a think cut of balsa wood. Balsa wood is a type of diffusive porous hardwood that is mainly composed of long prismatic cells[2, 3]. Its porosity can be up to > 90%[3]. The microstructure of balsa wood provides a good model for an air pocket under water and might be compared to some biological air pocket models as well, such as alveolar sacs.

4.2 Cavitation Thresholds at Pressure-Release Interfaces

4.2.1 Methods: Observations of Cavitation and Cavitation Probability

To create a pressure-release interface at the focus of the transducer, both the packing tape and the shrink film were fixed to a plastic holder. The dimensions of the holder were 4 cm in the axial direction, 4 cm in the lateral direction, and 8 cm in the elevational direction with respect to the transducer. It had an open acoustic window (4 cm*8 cm) facing the transducer. The tape and the film were both glued to the holder using epoxy (E-00NS, LOCTITE, USA) with their edges tightly sealed, creating an airtight volume inside the sealed volume. The adhesive side of the tape was glued to the holder, leaving the non-adhesive side facing the incident ultrasound waves. The shrink film was heated after the epoxy cured for a smooth and tight surface finishing. During experiments, the holder along with the sealed interface was positioned so that the interface was at the focus of the transducer and the surface of the interface was perpendicular to the propagation direction of the ultrasound. For the experiments where balsa wood was used as the pressure-release interface, a 2 cm*2 cm*0.5 cm wood block was glued to the 3-D motor positioner so that the water-wood interface was at the focus of the transducer. A high-speed camera was then used to observe the cavitation activities at the interfaces.

Five random spots at each pressure-release interface were selected to explore the potential discrepancy of the threshold curves. For each spot, 30 pseudo-monopolar peak positive

pulses were applied, focusing at the pressure-release interface. High-speed photography was then analyzed to observe the cavitation bubble clouds at the interface. The number of pulses where cavitation bubbles were generated was recorded. A probability value of cavitation was then calculated by dividing the number of pulses by the total number of 30. Various peak positive pressure levels were applied. Threshold curves were plotted with all the cavitation probability and pressure level data.

To test our hypothesis that the pressure-release interfaces we used resulted in a reflection coefficient of -1, we tried generating cavitation bubble clouds in a new focal area in free water with peak negative pulses that were generated by reflecting the peak positive pulses off the pressure-release interface. Plotting the intrinsic threshold curves on the peak positive pressures helped us test the hypothesis. Experiments were conducted with both the packing tape and the shrink film. The "reflecting and re-focusing" process was achieved by moving the pressure-release interface 1 cm towards the transducer in the axial direction. The resultant new focus was then moved 2 cm towards the transducer with respect to the original, geometric focus. 30 peak positive pulses were applied at each pressure level while various pressure levels were applied. High-speed photography was used to observe the cavitation bubbles generated at this new focus. Cavitation probability statistics were generated in the same method mentioned earlier. Threshold curves were plotted with all the probability and pressure levels data. This experiment was not performed for the balsa wood pressure-release interface because the re-focusing would not work due to uneven surface of the wood.

4.2.2 Results: Cavitation Bubble at Pressure-Release Interfaces and Cavitation Threshold Curves

A representative high-speed photograph of a cavitation bubble generated at the shrink film pressure-release interface is shown in Figure 4.1. The peak positive pressure of the applied positive pulse in this experiment was 20.8 MPa. We can see the cavitation bubble that was generated at the pressure-release interface. Its dimensions were within 0.5 mm for both the axial and the elevational direction.

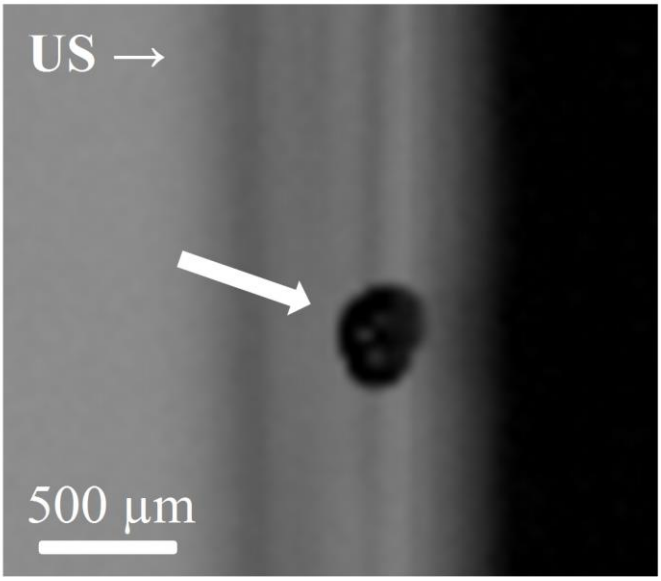

Figure 4.1 Representative photograph of a cavitation bubble generated at the shrink film pressure-release interface. The bubble was generated at the pressure-release interface and it is pointed out by a white arrow. The grey area on the left side is water and the dark area on the right side is the plastic holder. The vertical, blurred stripes show the edges of the plastic holder.

Cavitation threshold curves of the shrink film pressure-release interface are shown in Figure 4.2. For 5 different spatial spots at the pressure-release interface when the interface was at the focus, the mean pressure of the 50% cavitation probability point was 19.1 MPa, with a standard deviation of 0.6 MPa. Overall, the curves were consistent. For the cavitation generated at the re-focusing area in free water, the pressure of the 50% cavitation probability point was 32 MPa, which matches the intrinsic threshold measurements in previous studies[4-6]. This data

confirms that the reflection coefficient of the pressure-release interface is approximately -1, which proves our hypothesis. Also, the results show that the cavitation threshold at the pressure-release interface is lower than the intrinsic threshold in free water.

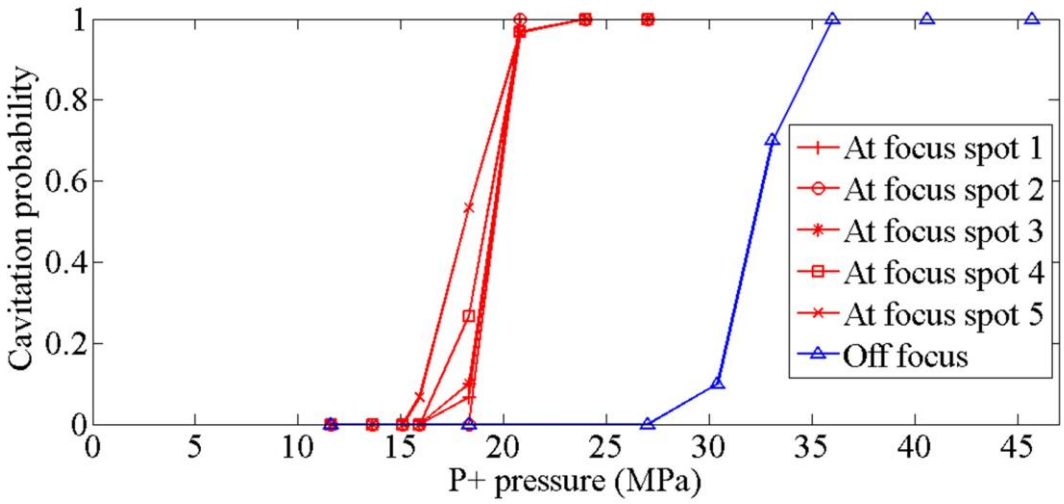

Figure 4.2 Cavitation threshold curves for the shrink film pressure-release interface. The 5 curves in red represent the cavitation threshold curves for the 5 different spatial spots when the interface was at the focus. The curve in blue represents the cavitation threshold curve for cavitation bubble generated at the re-focusing area in free water. Each probability data point had a sample size of 30.

Cavitation threshold curves of the packing tape pressure-release interface are shown in Figure 4.3. For this tape case, a reflection pressure loss of 22.69% was measured by comparing the focal peak positive pressure with the measured negative pressure at the re-focusing area. The pressure levels for this plot were corrected with this pressure loss rate. For 5 different spatial spots at the pressure-release interface when the interface was at the focus, the mean pressure of the 50% cavitation probability point was 15.3 MPa, with a standard deviation of 4.7 MPa. In this packing tape case, the threshold curves when the interface was at the focus varied more than those in the shrink film case. It might be because of the non-uniformity on the surface of the tape in terms of uneven thickness and possibly dirt attached to the non-adhesive side of the tape. For the cavitation generated at the re-focusing area in free water, the pressure of the 50% cavitation

probability point was 30 MPa, which again matches the intrinsic threshold measured previously. Similarly, the results show that the cavitation threshold at the pressure-release interface is lower than the intrinsic threshold in free water.

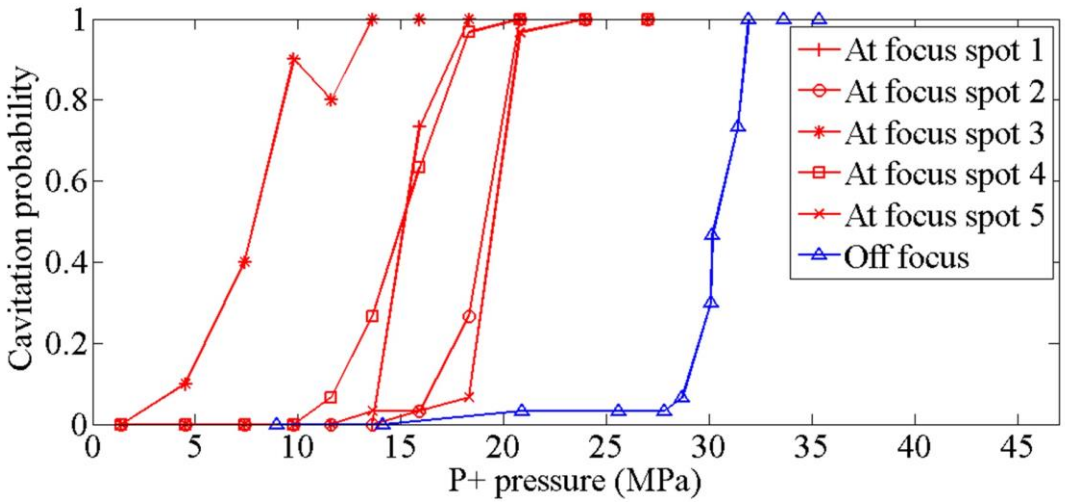

Figure 4.3 Cavitation threshold curves for the packing tape pressure-release interface. The 5 curves in red represent the cavitation threshold curves for the 5 different spatial spots when the interface was at the focus. The curve in blue represents the cavitation threshold curve for cavitation bubble generated at the re-focusing area in free water. Each probability data point had a sample size of 30.

Cavitation threshold curves of the balsa wood pressure-release interface are shown in Figure 4.4. For 5 different spatial spots at the pressure-release interface when the interface was at the focus, the mean pressure of the 50% cavitation probability point was 6.3 MPa, with a standard deviation of 0.2 MPa. The curves were consistent.

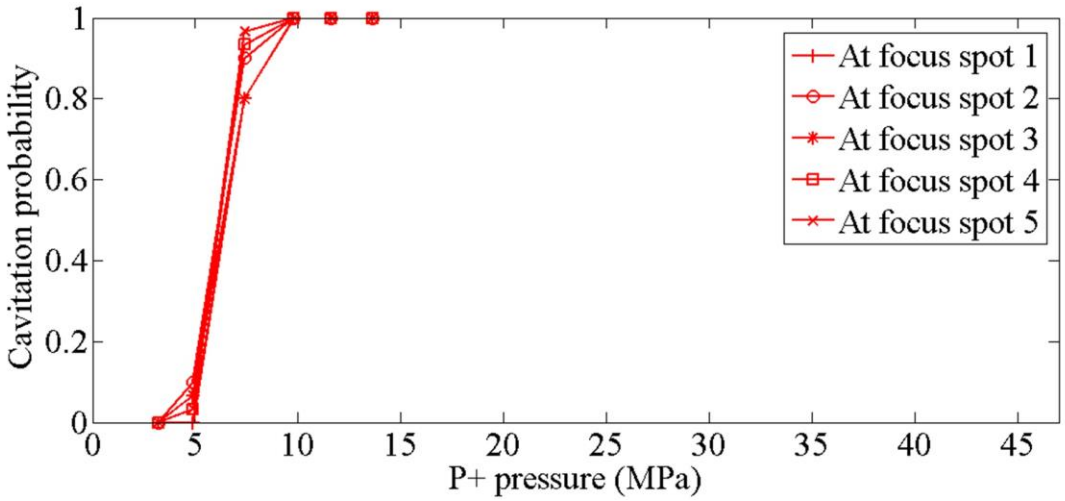

Figure 4.4 Cavitation threshold curves for the balsa wood pressure-release interface. The 5 curves in red represent the cavitation threshold curves for the 5 different spatial spots when the interface was at the focus. Each probability data point had a sample size of 30.

4.3 Cavitation Generated at Air Pocket Inclusion

To compare the cavitation effects generated by peak positive pulses and peak negative pulses on an air pocket/gas body within the ultrasound field, a balsa wood block was introduced within the field at different spatial points. These experiments were designed and conducted to provide experimental evidence and references for safety issues regarding an mm-sized gas body's existence within a therapeutic ultrasound field.

4.3.1 Methods: Balsa Wood Inclusion

A small rectangular block of balsa wood was glued to a thin shrink film by using the epoxy. The dimensions of the wood block were 3 mm*3 mm*3 mm. Water filled up the space behind the film to ensure the propagation of ultrasound waves. The frontal surface of the wood block was positioned at the focus initially, facing the transducer. Then, it was moved to 5 mm closer, 10 mm closer, 5 mm away, and 10 mm away from the transducer in the axial direction with respect to the focus. At each of the five locations, peak negative pulses with a focal peak negative pressure of 45 MPa and peak positive pulses with a focal peak positive pressure of 61

MPa were applied. High-speed photography was used to observe the cavitation effects on the balsa wood inclusion.

4.3.2 Results: Cavitation Generated at Balsa Wood Inclusion

Representative photographs of the balsa wood inclusion with peak positive and negative pulses applied when the inclusion was positioned at the focus are shown in Figure 4.5. Photographs on the left panel are three successive images of the balsa wood inclusion when a peak negative pulse was applied. On the right panel, three successive images of the balsa wood inclusion are shown when a peak positive pulse was applied. The same order applies for Figure 4.6, Figure 4.7, Figure 4.8, and Figure 4.9. White squares marked the edge of the balsa wood block so that potential cavitation bubbles can be differentiated from the wood since they both appeared dark in the image. Bold white crosses marked the location of the focus.

From Figure 4.5, for the balsa wood inclusion when a peak negative pulse was applied, cavitation bubbles appeared surrounding the surfaces of the balsa wood when the pulse arrived at the focus (0 μs). Then, the cavitation bubbles expanded from their original sizes at 18.9 μs. At 37.7 μs, the individual cavitation bubbles seemed to collapse into a big bubble cloud. When a peak positive pulse was applied, which was shown by the three successive images on the right panel, a relatively dense cavitation bubble cloud was generated on the frontal surface of the balsa wood at 0 μs when the peak positive pulse arrived at the focus. Then, it continued to evolve to a bigger size at 18.9 μs and 37.7 μs.

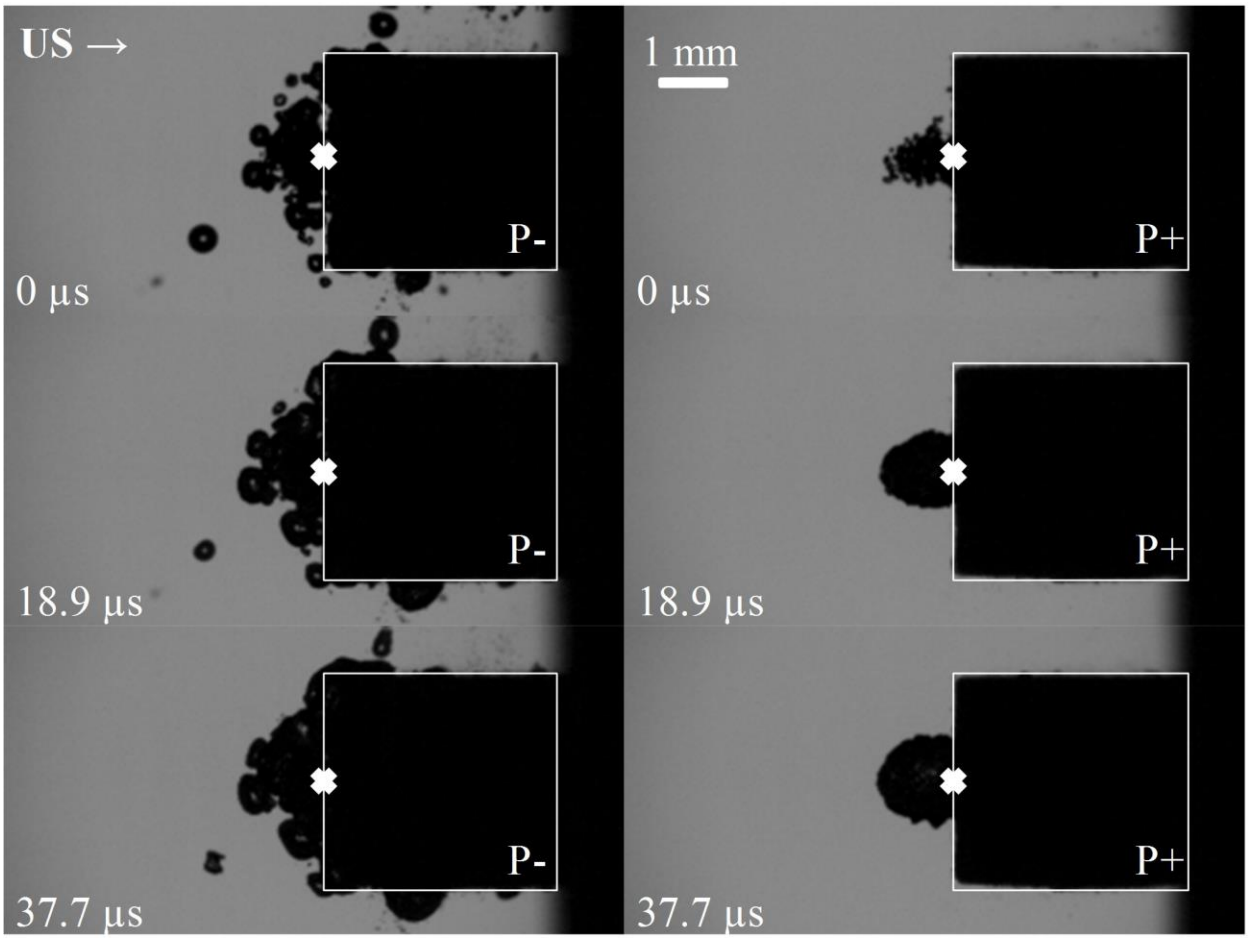

Figure 4.5 Representative photographs of the cavitation bubbles generated on the balsa wood inclusion when the inclusion was at the focus. Left panel: three successive images of the cavitation bubbles generated when a peak negative pulse was applied. Right panel: three successive images of the cavitation bubbles generated when a peak positive pulse was applied. White squares marked the edge of the balsa wood inclusion to help differentiate cavitation bubbles from the wood. Bold white crosses marked the focus of the transducer.

Representative photographs of the balsa wood inclusion with peak positive and negative pulses applied when the inclusion was positioned 5 mm closer to the transducer with respect to the focus are shown in Figure 4.6. When a peak negative pulse was applied, which was shown by three successive images on the left panel, cavitation bubbles were generated surrounding the surface of the balsa wood at 0 µs. Then, it kept expanding away from the balsa wood at 18.9 µs and 37.7 µs. When a peak positive pulse was applied, which was shown by three successive images on the right panel, cavitation bubble was barely observable.

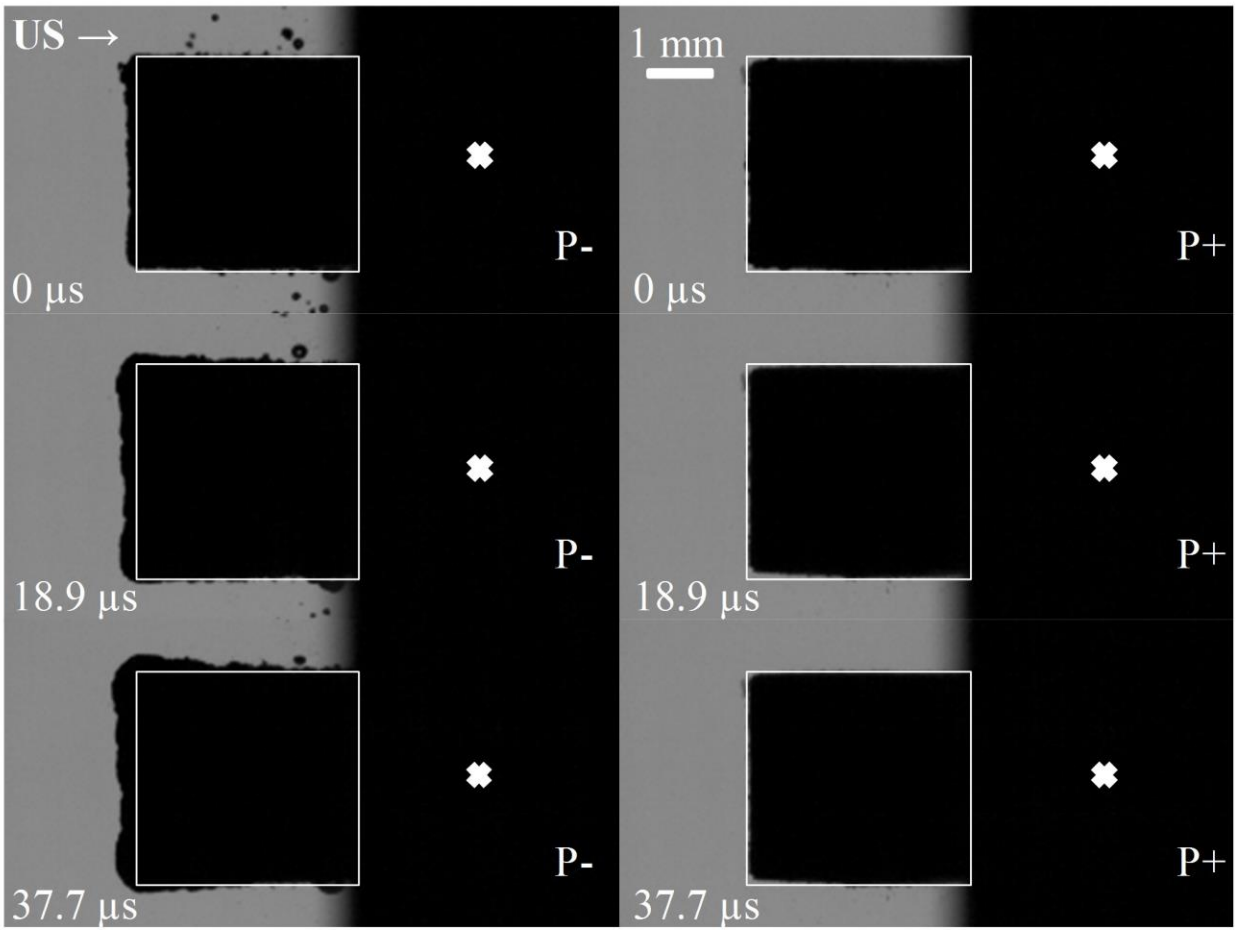

Figure 4.6 Representative photographs of the cavitation bubbles generated on the balsa wood inclusion when the inclusion was 5 mm closer to the transducer with respect to the focus. Left panel: three successive images of the cavitation bubbles generated when a peak negative pulse was applied. Right panel: three successive images of the cavitation bubbles generated when a peak positive pulse was applied. White squares marked the edge of the balsa wood inclusion to help differentiate cavitation bubbles from the wood. Bold white crosses marked the focus of the transducer.

Representative photographs of the balsa wood inclusion with peak positive and negative pulses applied when the inclusion was positioned 10 mm closer to the transducer with respect to the focus are shown in Figure 4.7. When a peak negative pulse was applied, which was shown by three successive images on the left panel, cavitation bubbles were barely observable. Some very small bubbles can be seen at 0 µs. They quickly disappeared at 18.9 µs. When a peak positive pulse was applied, there was no cavitation activity observable.

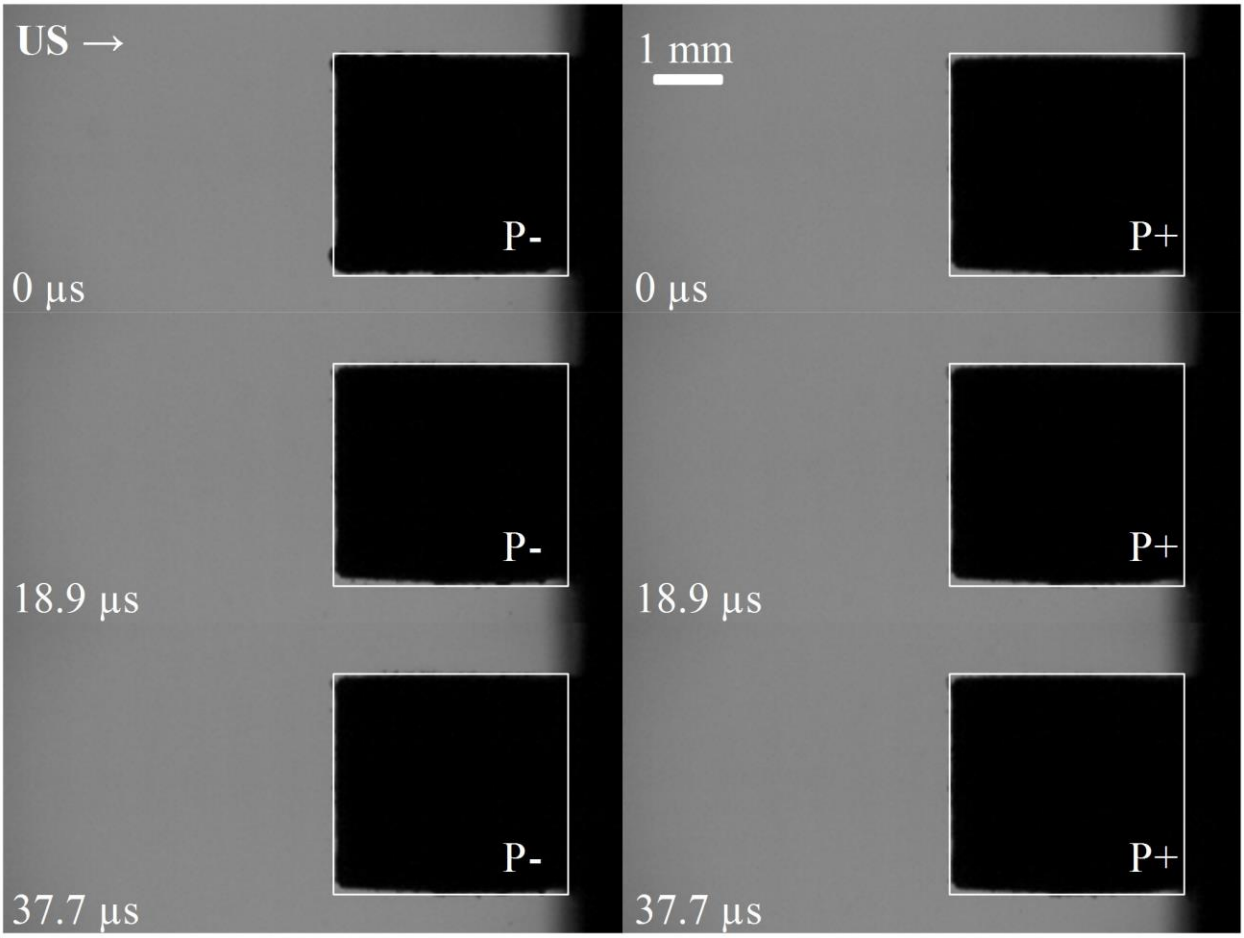

Figure 4.7 Representative photographs of the cavitation bubbles generated on the balsa wood inclusion when the inclusion was 10 mm closer to the transducer with respect to the focus. Left panel: three successive images of the cavitation bubbles generated when a peak negative pulse was applied. Right panel: three successive images of the cavitation bubbles generated when a peak positive pulse was applied. White squares marked the edge of the balsa wood inclusion to help differentiate cavitation bubbles from the wood.

Representative photographs of the balsa wood inclusion with peak positive and negative pulses applied when the inclusion was positioned 5 mm away from the transducer with respect to the focus are shown in Figure 4.8. When a peak negative pulse was applied, which was shown by three successive images on the left panel, a cavitation bubble cloud was generated at the focus and cavitation bubbles were also generated on the surface of the balsa wood. The expansion of the cavitation bubbles on the surface can be observed from 0 μs to 37.7 μs. When a peak positive pulse was applied, which was shown by three successive images on the right panel, there was no

cavitation at the focus. On the surface of the balsa wood, no obvious cavitation was observable either, except for some small incidental bubbles shown at 37.7 μs.

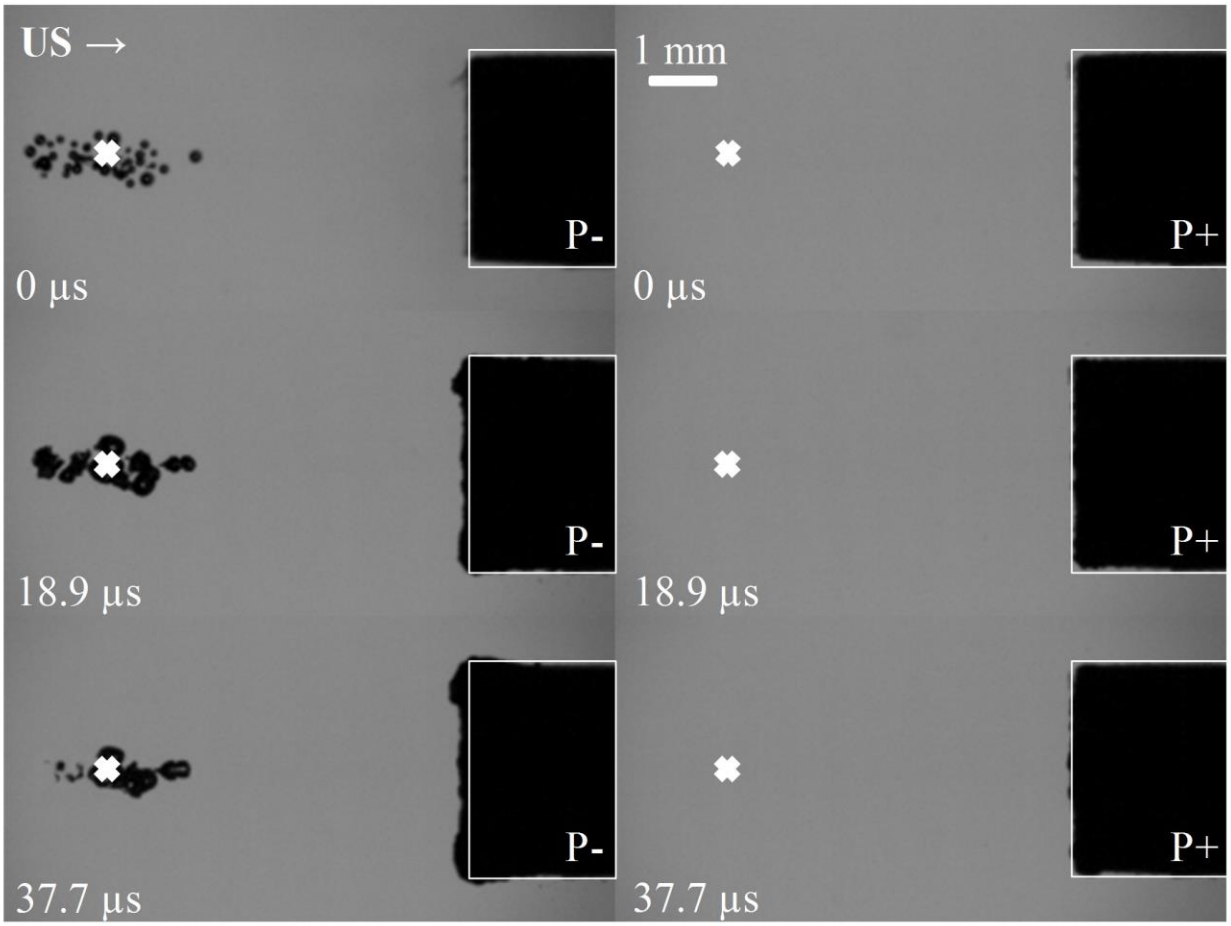

Figure 4.8 Representative photographs of the cavitation bubbles generated on the balsa wood inclusion when the inclusion was 5 mm away from the transducer with respect to the focus. Left panel: three successive images of the cavitation bubbles generated when a peak negative pulse was applied. Right panel: three successive images of the cavitation bubbles generated when a peak positive pulse was applied. White squares marked the edge of the balsa wood inclusion to help differentiate cavitation bubbles from the wood. Bold white crosses marked the focus of the transducer.

Representative photographs of the balsa wood inclusion with peak positive and negative pulses applied when the inclusion was positioned 10 mm away from the transducer with respect to the focus are shown in Figure 4.9. At this location, neither peak positive pulses nor peak

negative pulses was able to generate observable cavitation bubbles at the surface of the balsa wood.

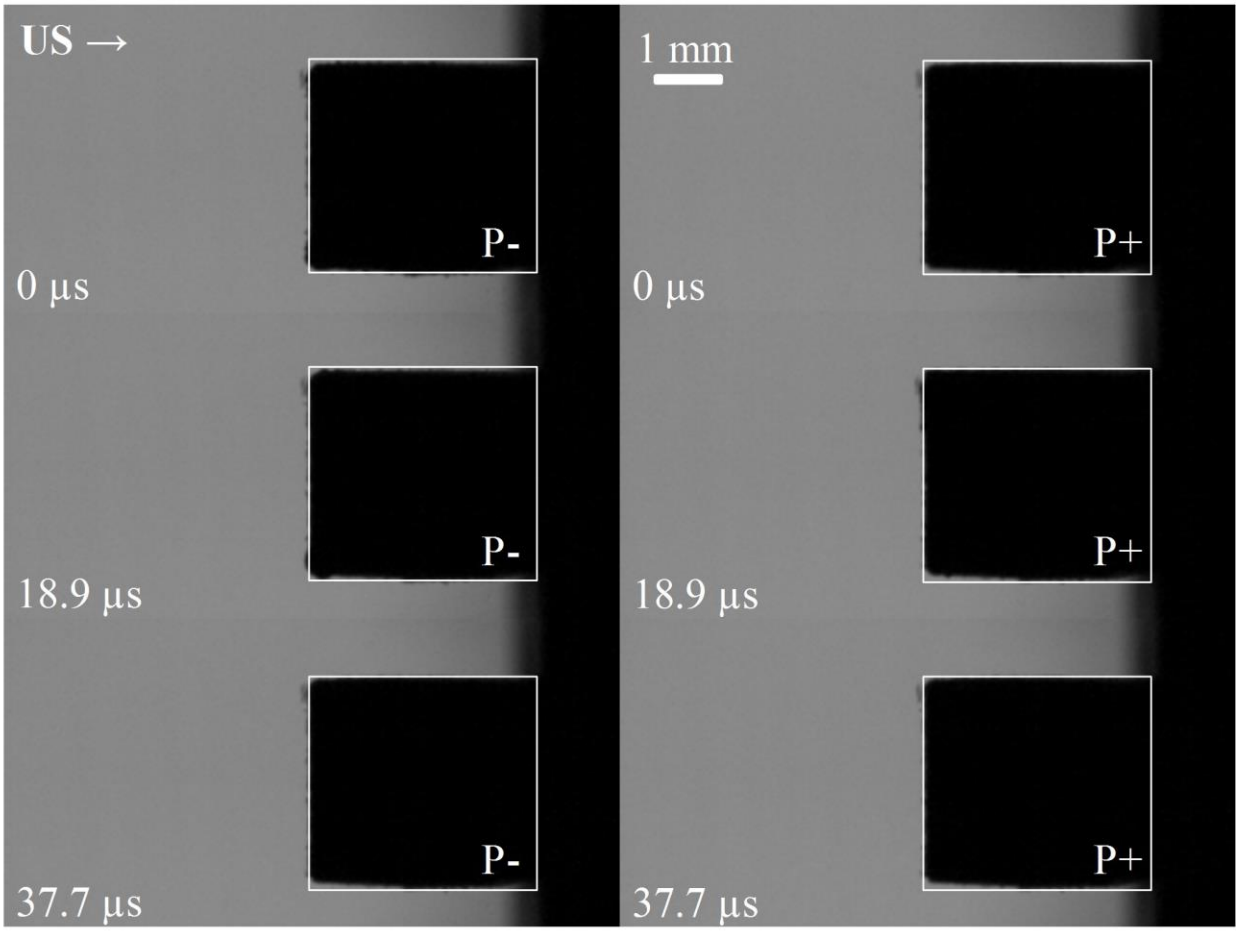

Figure 4.9 Representative photographs of the cavitation bubbles generated on the balsa wood inclusion when the inclusion was 10 mm away from the transducer with respect to the focus. Left panel: three successive images of the cavitation bubbles generated when a peak negative pulse was applied. Right panel: three successive images of the cavitation bubbles generated when a peak positive pulse was applied. White squares marked the edge of the balsa wood inclusion to help differentiate cavitation bubbles from the wood.

4.4 Cavitation Generated by Peak Negative Pulses and Peak Positive Pulses at Similar Pressure Levels

Normally, the full width half maximum (FWHM) of a pseudo-monopolar peak negative pulse is bigger than that of a peak positive pulse at a similar pressure level. To qualitatively

examine the difference of the cavitation bubble clouds due to the FWHM discrepancy, experiments are designed and conducted to observe and compare the bubble clouds.

4.4.1 Methods: Peak Negative Pulses at the Focus and Peak Positive Pulses Re-Focusing with Reflection

To generate cavitation bubble clouds at the focus with peak negative pulses, pseudo-monopolar peak negative pulses were applied. The peak negative pressures applied were 39.2 MPa, 46.3 MPa, and 48.6 MPa.

To generate cavitation bubble clouds with peak positive pulses at a new focus, pseudo-monopolar peak positive pulses were applied, and they were reflected by a pressure-release shrink film interface positioned at 1 cm closer to the transducer. The resultant new focus was 2 cm closer to the transducer. The peak positive pressures applied were 39.8 MPa, 45.8 MPa, and 48 MPa, which were at the same level as the peak negative pulses applied, respectively. High-speed photography was used to observe the cavitation bubble clouds.

4.4.2 Results: Cavitation Bubble Clouds Generated by Peak Negative Pulses and Reflected Peak Positive Pulses

Representative photographs of the cavitation bubble clouds generated by peak negative pulses and reflected peak positive pulses are shown in Figure 4.10. The cavitation bubble clouds generated at the focus with peak negative pulses are shown on the left panel. The size of the bubble cloud increased in both the axial dimension and the elevational dimension with increased peak negative pressures (from 39.2 MPa to 48.6 MPa). The cavitation bubble clouds generated at the re-focusing area with reflected peak positive pulses are shown on the right panel. With increased peak positive pressures, the size of the bubble cloud increased significantly in the axial dimension. In the elevational dimension, the increase was not that significant. When comparing

the cavitation bubble clouds generated by peak negative pulses and reflected peak positive pulses at same pressure levels, we can see that the clouds generated by peak negative pulses were bigger than those generated by reflected peak positive pulses in both the axial dimension and the elevational dimension.

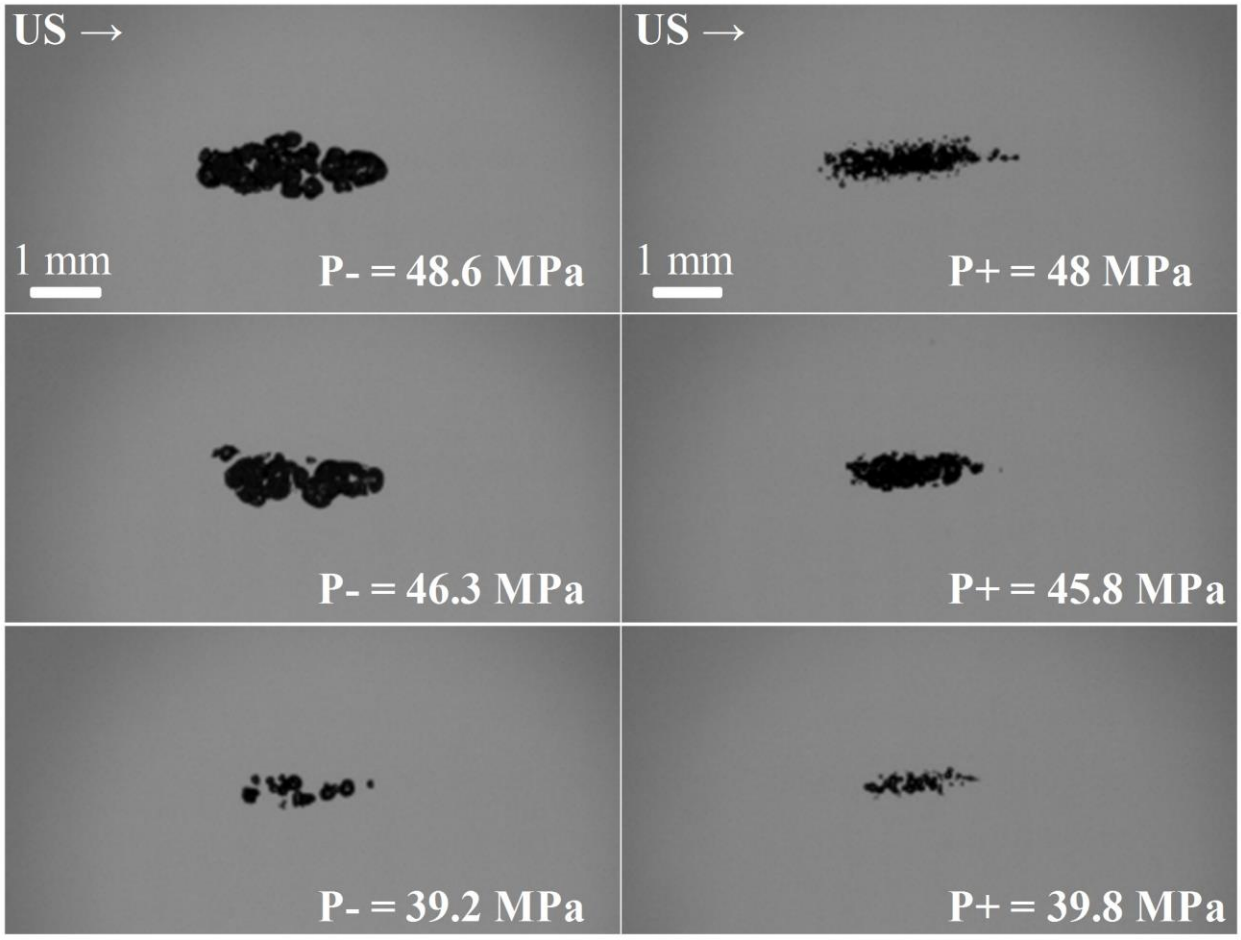

Figure 4.10 Representative photographs of the cavitation bubble clouds generated by peak negative pulses and reflected peak positive pulses. Left panel: cavitation bubble clouds generated at the focus by peak negative pulses whose focal negative pressure exceeded the intrinsic threshold. Right panel: cavitation bubble clouds generated at the re-focusing area by reflected peak positive pulses.

4.5 Discussion

In this chapter, cavitation thresholds at pressure-release interfaces were investigated with pseudo-monopolar ultrasound pulses. Several pressure-release models were explored including a

packing tape, a PVC shrink film, and a balsa wood model. We confirm that cavitation thresholds at interfaces are lower than the intrinsic threshold in free water, although the thresholds might differ from different materials. Hydrophilicity might be one of the many factors that cause the threshold difference. The materials we used are normally hydrophobic[7], which might cause cavitation nuclei to be trapped near the interface. The difference in hydrophilicity of different materials might lead to distribution change of the cavitation nuclei, resulting in a threshold change. In future studies, materials with more specific and controllable hydrophilicity can be investigated.

A balsa wood inclusion was introduced as a model to study the cavitation effects on gas pockets with pseudo-monopolar negative pulses and positive pulses. Although it might not be directly comparable to a specific clinical gas pocket situation, qualitative experimental evidence was presented regarding the differences of the cavitation bubble clouds generated by peak positive pulses and peak negative pulses with pressure levels generally used for therapeutic ultrasound. Cavitation bubbles generated by peak negative pulses were surrounding the surface of the balsa wood inclusion compared to the cavitation bubble cloud generated by peak positive pulses, which was very confined to the focal area. Also, cavitation bubbles were generated on the balsa wood inclusion with negative pulses at several spatial locations when there was no observable cavitation bubble with positive pulses. We think these experimental results could provide additional information regarding safety issues associated with therapeutic ultrasound.

4.6 References

1. Kinsler LE, Frey AR, Coppens AB, Sanders JV. Fundamentals of acoustics. Fundamentals of Acoustics, 4th Edition, by Lawrence E. Kinsler, Austin R. Frey, Alan B. Coppens, James V. Sanders, pp. 560. ISBN 0-471-84789-5. Wiley-VCH, December 1999.. 1999 Dec:560.

2. Vural M, Ravichandran G. Dynamic response and energy dissipation characteristics of balsa wood: experiment and analysis. International Journal of Solids and structures. 2003 May 1;40(9):2147-70.

3. Greil P, Lifka T, Kaindl A. Biomorphic cellular silicon carbide ceramics from wood: I. Processing and microstructure. Journal of the European Ceramic Society. 1998 Dec 1;18(14):1961-73.

4. Maxwell AD, Cain CA, Hall TL, Fowlkes JB, Xu Z. Probability of cavitation for single ultrasound pulses applied to tissues and tissue-mimicking materials. Ultrasound in medicine & biology. 2013 Mar 1;39(3):449-65.

5. Lin KW, Duryea A, Kim Y, Hall T, Xu Z, Cain C. Dual-beam histotripsy: A low-frequency pump enabling a high-frequency probe for precise lesion formation. IEEE transactions on ultrasonics, ferroelectrics, and frequency control. 2014 Feb;61(2):325-40.

6. Lin KW, Kim Y, Maxwell AD, Wang TY, Hall TL, Xu Z, Fowlkes JB, Cain C. Histotripsy beyond the intrinsic cavitation threshold using very short ultrasound pulses: Microtripsy. IEEE transactions on ultrasonics, ferroelectrics, and frequency control. 2014 Feb;61(2):251-65.

7. Asadinezhad A, Lehocký M, Sáha P, Mozetič M. Recent progress in surface modification of polyvinyl chloride. Materials. 2012 Dec 18;5(12):2937-59.

Chapter 5 Localized Currents Generated by Simultaneous Ultrasound and Oscillating Magnetic Fields

The generation of monopolar acoustic pulses could be beneficial for brain stimulation since monopolar peak positive pulses could potentially provide a strong positive pressure field that could be used directly or in combination with a magnetic field to achieve non-invasive brain stimulation. With minimal or no negative pressures, we could expect no cavitation effects, which is crucial for the safety of ultrasound-related systems.

The goal of this work is to study a new approach that combines ultrasound and an oscillating magnetic field simultaneously to generate a lower frequency current that could be used for non-invasive brain stimulation. The Lorentz force effect combines two high frequency fields (magnetic and acoustic particle velocity) to generate a low frequency current suitable for brain stimulation, whose duration of one complete, active cycle will be in the range of a TMS pulse. This allows us potentially to take advantage of strong focusing and deep penetration of high frequency ultrasound. Compared with conventional stimulation techniques, we expect this method to be highly localized, non-invasive and able to achieve greater penetration depth.

Based on previous studies[1, 2], we know that the current density (in μA/cm^2) vector at a certain point is given by

$$\boldsymbol{J} = \sigma \boldsymbol{V} \times \boldsymbol{B}, \qquad 5.1$$

where σ is the conductivity (in S/m) of the conducting medium, V is the particle velocity (in m/s) induced by ultrasound and B is the magnetic field (in T) vector at that point.

Theoretically, if V and B are oscillating at the same frequency, the resulting J consists of a DC (direct current) component and a high frequency (doubling) component, as shown in Figure 5.1. To achieve stimulation purposes, we are interested in the DC component of the currents. The magnitude of the DC component depends on the magnitude of the two original oscillating signals and the phase difference between the two. The relationship can be written as

$$J_{DC} = \frac{BV\cos\theta}{2}, \tag{5.2}$$

where B is the magnitude of the oscillating magnetic field, V is the magnitude of the oscillating particle velocity and θ is the phase difference between two signals. The high frequency component is given by

$$J_{HF} = \frac{BV\cos(2\omega t-\theta)}{2}, \tag{5.3}$$

where ω is the radian frequency of both velocity and magnetic field. From the equation, we can know that the magnitude of the high frequency component is only dependent on the magnitude of velocity and magnetic field.

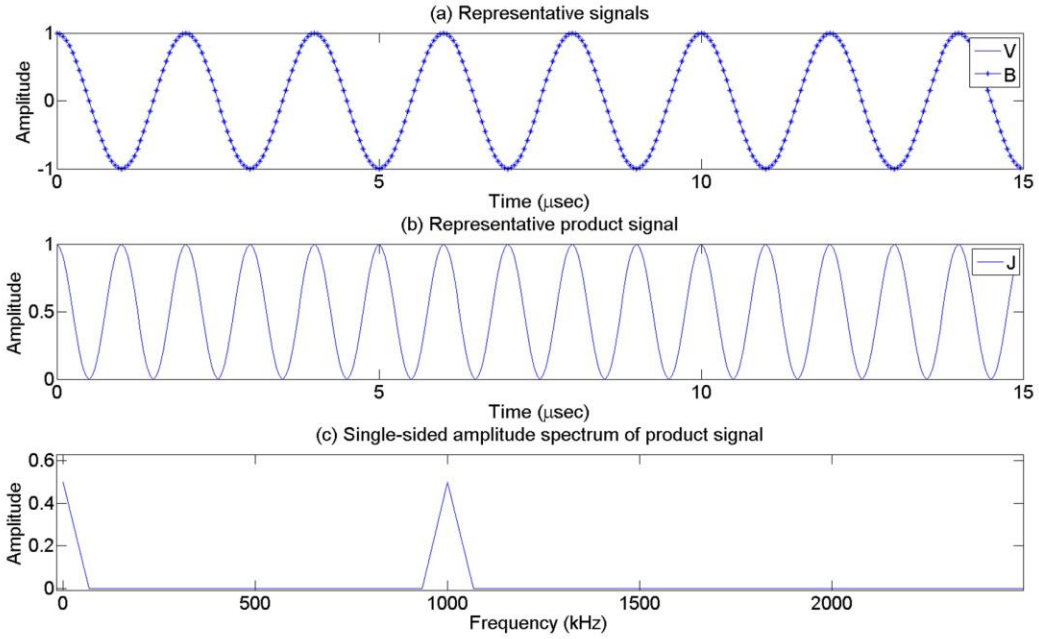

Figure 5.1 Representative signals of V, B, and J. (a) Representative signals of particle velocity (V) and oscillating magnetic field (B). Both are 500 kHz sinusoid with amplitude of 1. (b) Representative signal of the product (J) of V and B. The signal consists of a DC component (notice the shift upwards in amplitude) and a 1 MHz (doubling frequency) component. (c) Single-sided amplitude spectrum of product signal (J). There is a DC component with amplitude of 0.5 and a 1 MHz component with amplitude of 0.5.

The particle velocity field can be approximated as follows. Consider a "piston" ultrasound source with the condition of $a \gg \lambda$, where a is the radius of the source and λ is the wavelength of ultrasound. In its far field region, we can approximate the ultrasound wave to be a plane-traveling wave[3]. As a result, when a wave is propagating through a homogeneous medium with minimal attenuation, the particle velocity and ultrasound pressure are in phase with each other and their relationship is given by

$$\frac{P}{V} = \rho_0 c = Z, \qquad 5.4$$

where P is the pressure (in MPa) of ultrasound, ρ_0 is the density (in kg/m^3) of the medium, c is the sound speed (in m/s) in the medium and Z is the acoustic impedance (in MRayl). The relationship is analogous to Ohm's law. Under the approximations above, we can also determine

that the direction of the particle velocity is uniform and is parallel to the propagation direction of the ultrasound.

5.1 Current Density Distribution Simulation

5.1.1 Methods: FOCUS Simulation

To simulate the current density distribution created by the Lorentz force in a conducting medium, we first calculated a pressure field of an ultrasound transducer in its lateral-elevation plane using the Fast Object-oriented C++ Ultrasound Simulator (FOCUS, developed by McGough et al.[4, 5]). The simulation in this study was performed with Version 0.905 of FOCUS on version R2013a of MATLAB (MathWorks, Natick, MA). The transducer was defined as a "piston" ultrasound transducer with a diameter of 20 mm to match the transducer that was going to be used experimentally. The ultrasound wave was approximated by a 500 kHz sinusoid with the pressure magnitude calculated by FOCUS and the oscillating magnetic field was also approximated by a 500 kHz sinusoid with the field strength magnitude provided by our electromagnet apparatus. Then, numerical calculations using equations 5.1 and 5.4 were performed in MATLAB to output results of the current density distribution spatially and temporally. At the center spatial point, we assumed that the two signals were perfectly in phase and their directions were perpendicular to each other.

5.1.2 Results: Current Density Distribution

The FOCUS simulations produced a 2D image of the pressure field in the lateral-elevation plane generated by the "piston" transducer, as shown in Figure 5.2. The field of view was the size of the measurement chamber in the lateral-elevation plane. The distance in axial

direction was 6.5 cm, which was the distance between the transducer and the measurement chamber during experiments.

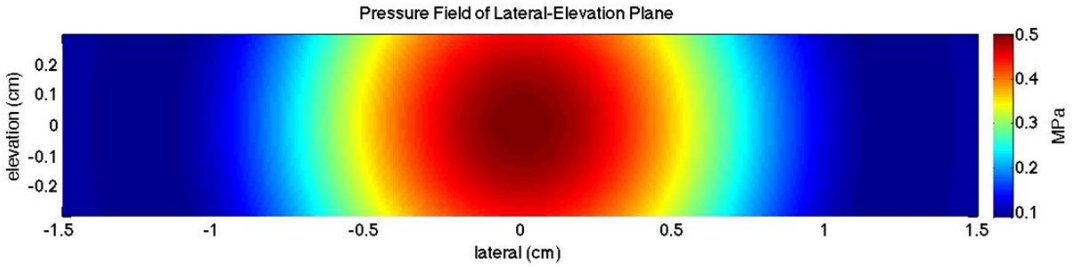

Figure 5.2 The 2-D pressure field generated by the 500 kHz transducer. The field of view was the size of the measurement chamber in lateral-elevation plane, generated in FOCUS.

We then simulated how current density vectors changed with time in a full cycle, which was from 0 μs to 2 μs (corresponding to 500 kHz frequency), in the measurement chamber volume. We only simulated the volume inside the measurement chamber because the chamber isolated the saline solution from surrounding water in the tank so that there were charged particles only in the chamber volume. Ultrasound waves oscillated along the axial direction while the magnetic field was oscillating along the elevation direction. As a result, current density vectors were generated along the lateral direction. Figure 5.3 shows a diagram of the simulated volume indicating the location of the planes shown in Figure 5.4. Figure 5.4 shows orthogonal slices of the calculated current density magnitude. The 0 μs time point was defined as the time when the peak positive pressure (P+) of ultrasound was right at the center of the volume inside the chamber axially and the oscillating magnetic field strength was at its maximum. Figure 5.5 shows how the magnitude of a single current density vector changed with time at the center spatial point of the volume. Besides its temporal behavior, the single-sided frequency spectrum of the amplitude was also plotted. The plot shows a DC component and a high frequency AC component, matching our theoretical predictions.

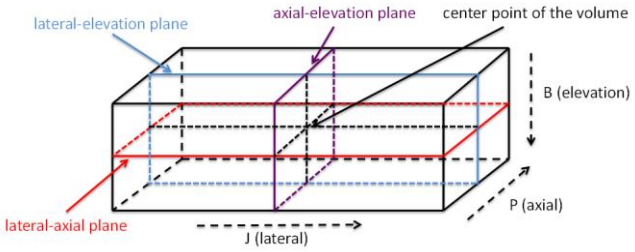

Figure 5.3 A representative diagram showing the simulated volume. The diagram is showing the measurement chamber (black lines), a central lateral-axial plane (red), a central lateral-elevation plane (light blue) and a central axial-elevation plane (purple). Three planes intersected at the center spatial point of the volume. Current density (J) was generated in the lateral direction when ultrasound pressure (P) was applied along the axial direction and the magnetic field (B) was applied along the elevation direction.

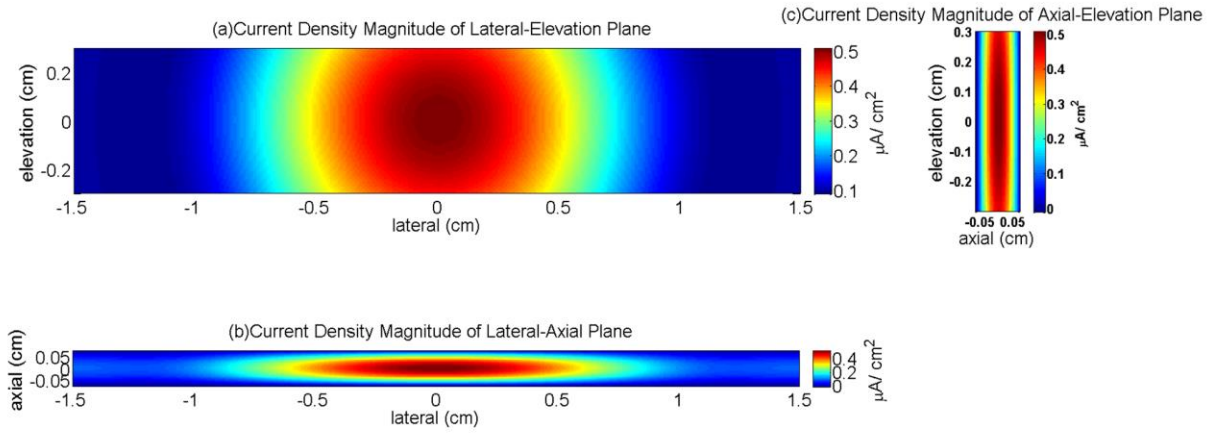

Figure 5.4 Simulated current density distribution in three slices. The figure shows that the current density magnitude of lateral-elevation plane had the same pattern as that in the ultrasound pressure field image, as our theory predicted. (b) Center slice of the current density magnitude along the lateral-axial plane. (c) Center slice of the current density magnitude along the axial-elevation plane. For (a)(b)(c), the maximum current density magnitude was around 0.5 μA/cm^2. The orientation of three simulated planes was shown in Figure 5.3.

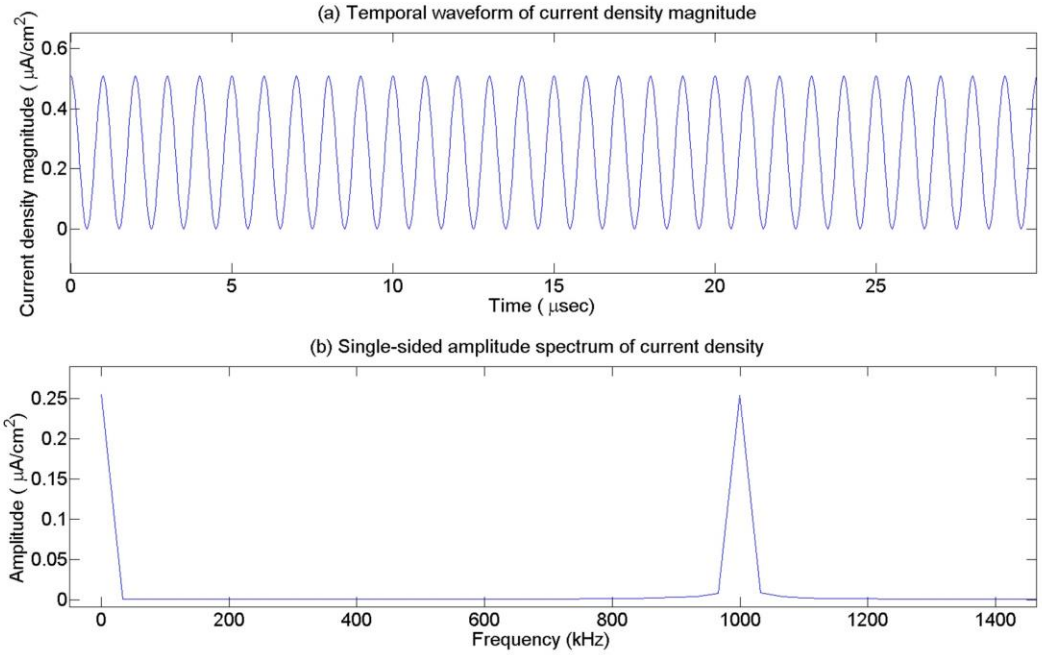

Figure 5.5 Simulated magnitude of a current density vector and its amplitude spectrum. Note that the waveform oscillated between around 0.5 μA/cm^2 and 0, which indicated that it had a DC component. (b) Single-sided amplitude spectrum of current density. There was a DC component with amplitude of 0.25 μA/cm^2 and a 1 MHz component with amplitude of 0.25 μA/cm^2.

The simulation results showed that, when the peak positive pressure (P+) was 0.50 MPa and the magnitude of the oscillating magnetic field was 4.3 mT, the maximum current density value in the volume was 0.51 μA/cm^2. Because there is a linear relation between the pressure magnitude, conductivity and the current density value, 1 μA/cm^2 current density should be expected when the ultrasound pressure is 10 MPa assuming the conductivity value of human gray matter to be 0.28 S/m[6]. The current density value with a higher pressure, which is around 10 MPa, is at the same level as that measured in human patients' scalp with TMS[7].

5.2 Induced Currents Measurements

5.2.1 Methods: Experimental Setup

To validate the above simulation experimentally, we constructed an apparatus to measure the current signal created by the interaction of ultrasound waves with an oscillating magnetic field. A schematic illustration of the experiment setup is shown in Figure 5.6. The magnetic field was created by a custom-made electromagnet. We used a N87 ferrite core (TDK, Tokyo, Japan) with an initial permeability of 2200, an effective length of 213.9 mm and an effective cross-sectional area of 216.7 mm^2. A 7 mm-wide gap was cut in the ferrite core, so a homogeneous magnetic field could be generated in the gap space. A thick wire (12 AWG, Bulkwire, Yorba Linda, CA) was wrapped around it with 33 turns and the electromagnet was driven by a power amplifier (Model 1040L, Electronics & Innovation, Rochester, NY) in line with a resonant matching circuit tuned to the frequency range of the ultrasound wave. We placed a thin measurement chamber made of cylindrical heat shrink tubing (Polyolefin, 1/8'', 3M, Maplewood, MN) in the gap, filling with 3% saline solution. We tested the conductivity of the solution to be around 3.5 S/m. The saline chamber was accommodated in the gap of the electromagnet, as shown in Figure 5.6. (Note that the same type of chamber was used in A. Montalibet et al.'s study[1] but we modified the dimensions, so it could fit in the gap of the electromagnet.) The center part of the tube was in rectangular shape, whose inner dimensions were 1.5 mm along the axial direction (half wavelength of generated ultrasound wave in its propagation direction), 6 mm in elevation direction (direction of the magnetic field) and 3 cm in lateral direction (direction of the generated current density). The extremities of the tube remained the original cylindrical shape and were connected to extended flexible tubes by plastic connectors, which were not shown in Figure 5.6 for simplicity.

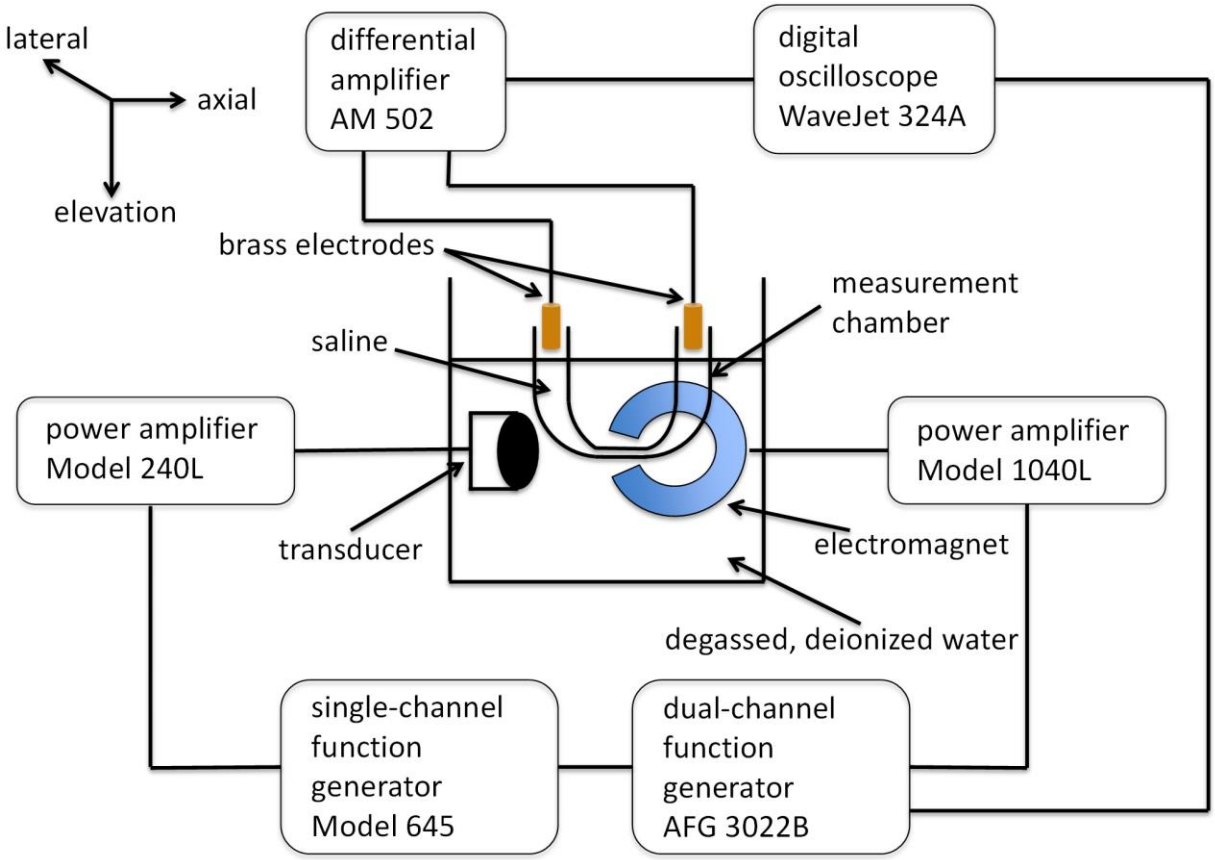

Figure 5.6 A diagram of the experimental setup. A 500 kHz ultrasound transducer was driven by a power amplifier that was connected with a function generator. An electromagnet was also driven by a power amplifier that was connected with another function generator. Two function generators and an oscilloscope were synchronized. A water tank was filled with degassed, deionized water. The transducer and the electromagnet were submerged in the water tank. A measurement chamber was also submerged in the water tank with its two extremities outside of water. The chamber was filled with saline solution. Brass electrodes were put in saline and connected to a current sensing circuit. The circuit was then connected to a differential amplifier, which was connected with the oscilloscope.

A custom-made unfocused "piston" ultrasound transducer with a 500 kHz center frequency was placed in front of the assembly such that it created a pressure field in the gap region of the electromagnet in the direction (axial) perpendicular to the magnetic field (elevation) and to the saline filled tube (lateral). The transducer was driven by a RF power amplifier (Model 240L, Electronics & Innovation, Rochester, NY). Also, a dual channel arbitrary/function generator (AFG 3022B, Tektronix, Beaverton, OR) and a single channel 50

MHz function/arbitrary waveform generator (Model 645, Berkeley Nucleonics Corp, San Rafael, CA) were used to generate driving signals to both power amplifiers mentioned above and a trigger signal to a 200 MHz, 4-channel oscilloscope (WaveJet 324A, LeCroy, Chestnut Ridge, NY). It was verified by a needle hydrophone (HNR-0500, ONDA, Sunnyvale, CA) that the presence of both the electromagnet and the measurement chamber did not affect the ultrasound field significantly. We calculated a maximum magnetic field strength of about 4.3 mT in the gap space with a 500 kHz center frequency.

A pair of brass electrodes was placed at two ends of the flexible tube to detect any induced currents. The electrodes were connected to a current sensing circuit. The circuit consisted of a resistor that was connected in series with the electrodes and a capacitor connected in parallel. The resistor was to provide a return path for any generated current and its resistance was 1/10 of the impedance of the medium. The capacitance was 0.068 μF. (Note that this RC circuit acted like a low pass filter.) Then, the voltage across the resistor was measured with a differential amplifier (AM 502, Tektronix, Beaverton, OR) whose input impedance was 1 MOhm. Finally, the amplifier was connected to a digital oscilloscope, synchronized with the function generator trigger signal. The electromagnet, the transducer and the measurement chamber were submerged in a water tank filled with degassed, deionized water for transmission of the ultrasound waves.

We collected 256 averages of the current signal with a full bandwidth (200 MHz). We performed experiments under the following scenarios. 1) The ultrasound transducer and the electromagnet were both turned on and fixed at the right position, 2) the ultrasound transducer was turned on while the electromagnet was turned off, 3) the ultrasound transducer was turned off while the electromagnet was turned on and 4) the ultrasound transducer and the

electromagnet were both turned on but the transducer was moved out of the functional region and there was a plastic plate (1.3 cm thick) blocking its wave propagation.

Practically, it would be difficult and inaccurate to directly detect a DC signal by inserting electrodes into saline because of electrochemical effects on the electrodes and excessive low frequency drifting noise. Instead, we induced and detected a low frequency (3 kHz and 4 kHz) AC current that would be suitable for neural stimulation, as we mentioned earlier. To achieve that, we shifted the frequency of the oscillating magnetic field to be several kHz off the center frequency of the ultrasound. By doing so, the induced current consisted of a low frequency (difference of two frequencies) component and a high frequency (sum of two frequencies) component. We Fourier transformed the observed signal to analyze its frequency contents.

5.2.2 Results: Measured De-Modulated Currents

A calibration of the ultrasound transducer was conducted by using a needle hydrophone to measure an ultrasound pressure waveform in degassed water. The hydrophone was fixed at around 6.5 cm away from the transducer. The calibration result is shown in Figure 5.7.

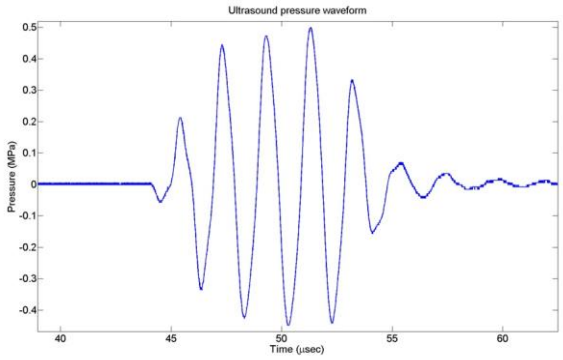

Figure 5.7 A representative 4-cycle ultrasound pressure waveform. The waveform was from the 500 kHz “piston” transducer at a peak positive pressure level of 0.50 MPa via direct hydrophone measurement.

For current measurement, we first tried inducing and detecting a 4 kHz current. The results are shown in Figure 5.8. The ultrasound pressure wave was oscillating at 500 kHz and

driven with 3000 cycles. The peak positive pressure (P+) was around 0.50 MPa and the peak negative pressure (P-) was around 0.49 MPa. The magnetic field was oscillating at 496 kHz, also driven with 3000 cycles and with maximum field strength of 4.3 mT. To verify the source of the induced current, the electromagnet and the ultrasound transducer were turned off individually, as mentioned in Methods. No signal of interest was observed in either case, as shown in Figure 5.8. However, a current signal was successfully observed when ultrasound and magnetic field were both turned on and fixed at the right position. There was a single peak at 4 kHz as expected. The amplitude was 0.34 µA/cm^2. To verify that we were not simply detecting electromagnetic noise from the interaction between the ultrasound apparatus and the electromagnet, we also tried moving the ultrasound transducer out of the functional region and placed a plastic plate to block the propagation path of ultrasound waves while the transducer was still turned on in the water tank. There was no detected signal of interest in this case, either.

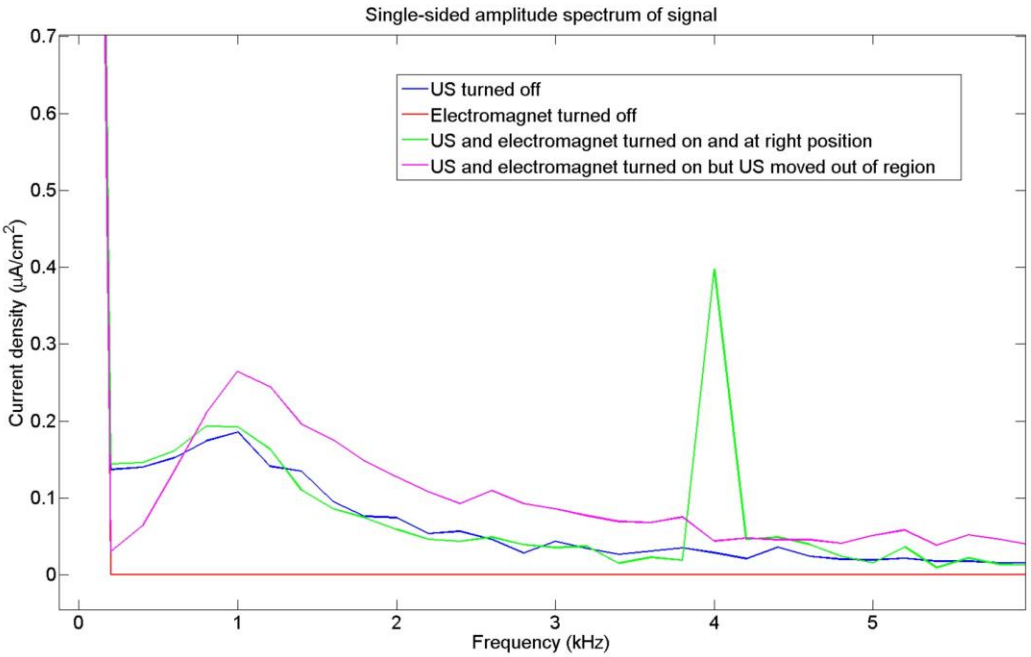

Figure 5.8 The single-sided amplitude spectrum of the detected signals. The green line represents the signal when both the ultrasound transducer and the electromagnet were turned on and fixed at

the right position. A 4 kHz component with a magnitude of 0.34 µA/cm^2 was observed. The background noise had a peak at 1 kHz because the -3dB low pass filter cut-off frequency on the amplifier was set to be 1 kHz. The blue line represents the signal when the ultrasound transducer was turned off. The red line represents the signal when the electromagnet was turned off. The magenta line represents the signal when both the ultrasound transducer and the electromagnet were turned on, but the transducer was moved out of the functional region with a plastic plate blocking the propagation of ultrasound waves.

To test the consistency of the amplitude of the induced currents, we tried inducing and detecting a 3 kHz current by setting the frequency of the oscillating magnetic field to be 497 kHz. The results are shown in Figure 5.9. The amplitude of the 3 kHz current was 0.39 µA/cm^2, which was consistent with the 4 kHz current. This result proved that, theoretically, by modulating the difference frequency between the ultrasound waves and the oscillating magnetic field, we could generate currents in any frequency. And their magnitude should be consistent.

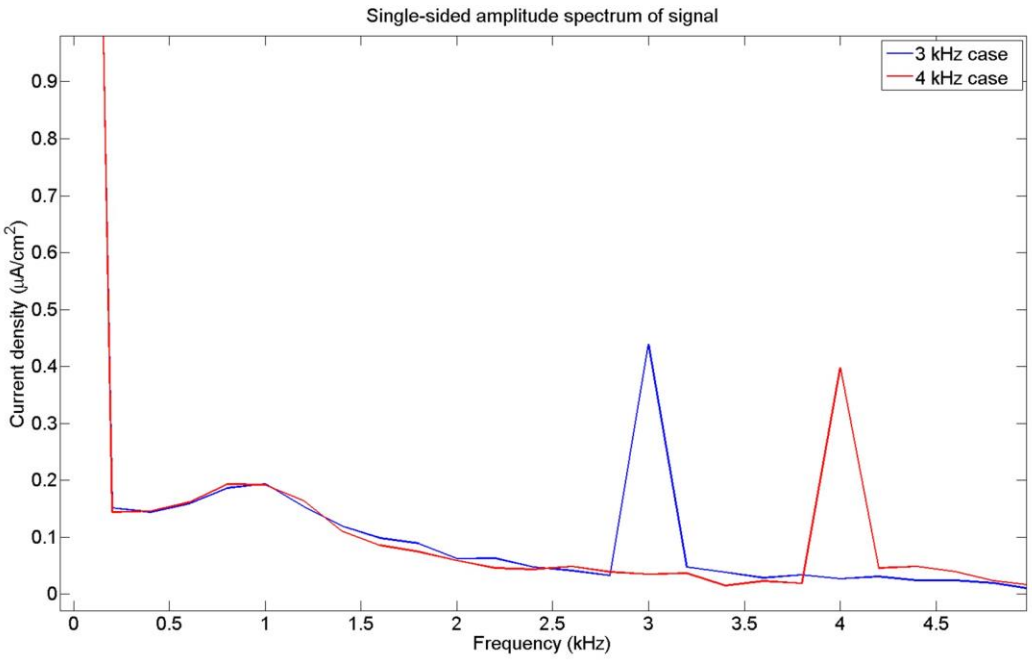

Figure 5.9 The single-sided amplitude spectrum of the detected signals. The red line represents the signal with a 4 kHz component with a magnitude of 0.34 µA/cm^2. The blue line represents the signal with a 3 kHz component with a magnitude of 0.39 µA/cm^2.

To test that the magnitude of the induced current is linear with the conductivity change based on equation 5.1, we tried comparing the amplitude of the signal in a 3% saline

environment and a 9% saline environment. The results are shown in Figure 5.10. For 3% saline, the conductivity was 3.5 S/m. The amplitude of the signal was 0.34 µA/cm^2. For 9% saline, the conductivity was 13.5 S/m. The amplitude of the signal was 1.7 µA/cm^2. Thus, a 3.9-fold increase in the conductivity resulted in a 5.0-fold increase in the current.

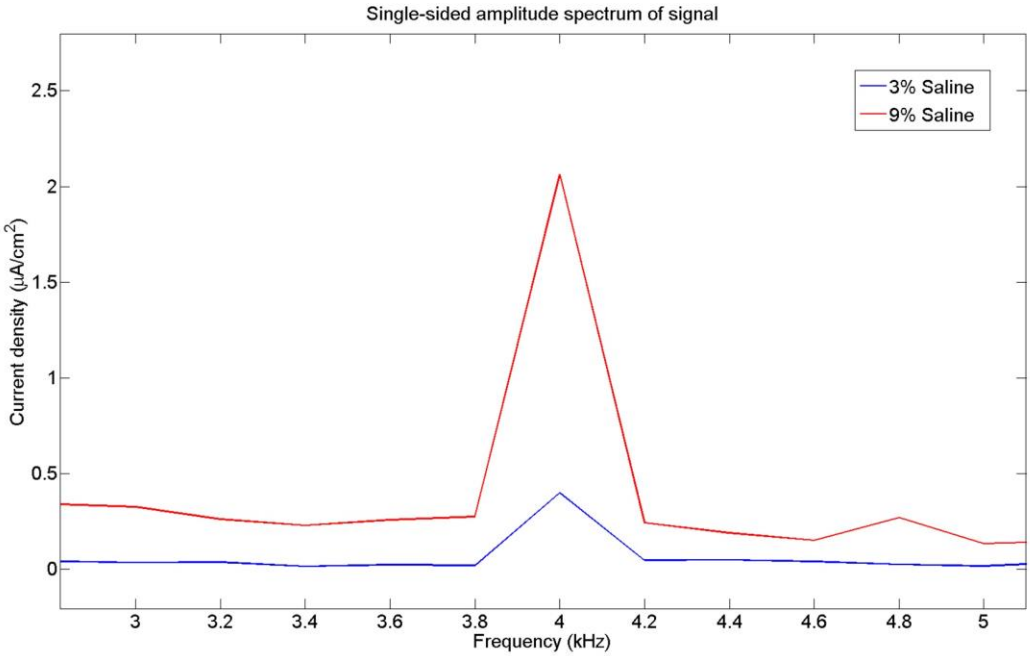

Figure 5.10 The single-sided amplitude spectrum of the detected signals. Red line represents the signal with a 4 kHz component with a magnitude of 1.7 µA/cm^2 in a 9% saline environment, which corresponds to conductivity of 13.5 S/m. Blue line represents the signal with a 4 kHz component with a magnitude of 0.34 µA/cm^2 in a 3% saline environment, which corresponds to conductivity of 3.5 S/m.

The induced current density we measured was about 0.34 µA/cm^2 at 4 kHz and 0.39 µA/cm^2 at 3 kHz, which were on the order of the simulation results of 0.26 µA/cm^2. We considered the results matched well especially given the small scale of the predicted current value.

5.3 Discussion

In this chapter, we have demonstrated that de-modulated low frequency currents can be induced by simultaneous ultrasound and an oscillating magnetic field. Our aim was to generate a current whose frequency was in the range of a TMS pulse (~3 kHz). Experimentally, currents at 4 kHz and 3 kHz were successfully induced and measured. Furthermore, experimental results matched well with our simulation results in terms of the current density values, which proved that our theoretical model was correct. However, we were unable to observe a pure DC signal because of excessive low-frequency background noise. Figure 5.8 suggested a 1/f relationship between the noise level and the frequency. When the power amplifier was turned off, the 1/f noise was dramatically reduced, indicating that the noise source was primarily the power amplifier. Therefore, we modulated the frequency of the oscillating magnetic field so that the induced current would be at a frequency where there was much less background noise.

In our experiments, there were some factors that could cause the difference between the simulation results and the experimental results. We took some of them into consideration quantitatively when we performed the simulation to maximally approximate the experimental conditions. For instance, we calibrated the pressure decrease of the ultrasound field with and without the electromagnet and the measurement chamber. Also, we considered the ultrasound pressure drop in axial direction inside the measurement chamber because the thickness of the chamber was a half wavelength of ultrasound. However, there were some factors that we couldn't evaluate quantitatively. For example, the magnetic field strength was calibrated when the electromagnet was setup in normal air condition. Submerging the electromagnet in the water tank might affect the actual field strength. As a result, this might cause the current density induced during experiments to be different from the simulated values. Another factor was that by

using the half-wavelength thick chamber, different spatial points in axial direction inside the chamber would have phase difference of acoustic particle velocity since ultrasound was propagating through the conducting medium while the magnetic field strength had no phase difference for different spatial points. In our study we assumed that there was no phase difference of acoustic particle velocity between the center spatial points and other spatial points because the region with higher ultrasound pressure was very small so that the phase difference for those points in that region should be small as well. Therefore, it could be ignored. However, the difference could affect the experimental results regarding the current density values.

Looking forward, we expect that ultrasound and magnetic fields together will be able to stimulate brain tissue non-invasively with high penetration depth as well as specificity, by leveraging the features of focused ultrasound technology. Theoretically, with higher ultrasound pressure and bigger magnetic field strength, we could achieve the equivalent level of current density measured during TMS treatments of human heads. This will allow future development of an exquisitely accurate, non-invasive stimulation system with much higher penetration depth than TMS or other methods such as tDCS (transcranial Direct Current Stimulation)[8].

5.4 References

1. Montalibet A, Jossinet J, Matias A, Cathignol D. Electric current generated by ultrasonically induced Lorentz force in biological media. Medical and Biological Engineering and Computing. 2001 Jan 1;39(1):15-20.

2. Norton SJ. Can ultrasound be used to stimulate nerve tissue?. Biomedical engineering online. 2003 Dec;2(1):6.

3. Wu J, Nyborg WL. Ultrasound, cavitation bubbles and their interaction with cells. Advanced drug delivery reviews. 2008 Jun 30;60(10):1103-16.

4. Kelly JF, McGough RJ. A time-space decomposition method for calculating the nearfield pressure generated by a pulsed circular piston. IEEE transactions on ultrasonics, ferroelectrics, and frequency control. 2006 Jun;53(6):1150-9.

5. McGough RJ, Samulski TV, Kelly JF. An efficient grid sectoring method for calculations of the near-field pressure generated by a circular piston. The Journal of the Acoustical Society of America. 2004 May;115(5):1942-54.

6. Latikka J, Kuurne T, Eskola H. Conductivity of living intracranial tissues. Physics in Medicine & Biology. 2001 Jun;46(6):1611.

7. Wagner T, Gangitano M, Romero R, Théoret H, Kobayashi M, Anschel D, Ives J, Cuffin N, Schomer D, Pascual-Leone A. Intracranial measurement of current densities induced by transcranial magnetic stimulation in the human brain. Neuroscience letters. 2004 Jan 9;354(2):91-4.

8. Gandiga PC, Hummel FC, Cohen LG. Transcranial DC stimulation (tDCS): a tool for double-blind sham-controlled clinical studies in brain stimulation. Clinical neurophysiology. 2006 Apr 1;117(4):845-50.

Chapter 6 Conclusions and Future Work

6.1 Future Work in Frequency Compounding

As mentioned in Chapter 2, the optimization of monopolar acoustic pulses still requires more work and efforts in various aspects. For a monopolar peak positive pulse, a higher peak positive pressure with an even lower peak negative pressure is desired. Also, a driving system that allows us to apply successive monopolar acoustic pulses with shorter time delays can be developed. This could potentially allow us to use these monopolar pulses to generate lesions in a 3-D volume more efficiently.

To be specific, these works could be done in the future. 1) The improvement of the construction of individual elements. This could involve the implementation of new transducer materials and the testing of new matching layer models with better performance metrics such as the pressure output and the bandwidth. 2) The improvement of the optimization routine. In the study described earlier, the optimization routine used was based on the Monte-Carlo method, which took advantage of the computing ability of computers but remained trivial in math. A more advanced optimization algorithm could be developed to take Gaussian pulses and even realistic pressure waveforms as inputs and output a more optimal solution, rather than provide a local optimal solution based on each optimization trial. 3) The improvement of the driving system. This could be done by developing a brand-new driving system with an advanced structure which might be different from the existing current driving system. Secondly, another possibility is that we could design a new transducer with several subsections where each subsection is responsible for generating an independent monopolar pulse. Applying different

pulsing sequences could be achieved by modifying the firing events of those subsections of the overall transducer. Precise timing control of successive pulses could be achieved in this way as well.

Using monopolar acoustic pulses as imaging pulses could also be a very beneficial application that we can work on in the future. To achieve it, linear arrays could be developed to cover a more uniform region as the imaging target. Further development of monopolar pulses at different resonant frequencies could greatly help generate an overall monopolar imaging pulse with a strong steering ability and a more uniform pressure distribution, which are important for obtaining high-quality images.

6.2 Future Work in the Study of Pressure-Release Interfaces

Future work could be done to investigate the effects of specific hydrophilicity of the interface materials on the cavitation thresholds at pressure-release interfaces. This could be realized by applying hydrophilic sprays onto hydrophobic interfaces and then comparing the resultant cavitation threshold differences. Also, future work could be done to investigate the cavitation bubble clouds generated by two ultrasound waves which are propagating towards each other. This might help look at the clinical situation where a high amplitude positive pulse gets reflected and then becomes a peak negative pulse. If there is another counter propagating negative pulse and they add constructively, cavitation bubbles can be generated if the overall peak negative pressure exceeds the intrinsic threshold, which means that cavitation could appear somewhere never expected before. The negative pressures of both the peak negative pulses don’t necessarily have to exceed the intrinsic threshold. This could be realized by applying a peak negative pulse following a peak positive pulse which will be reflected by a pressure-release

interface. The peak negative pulse should be focusing at the resultant “new focus” from the reflection of the positive pulse.

6.3 Future Work in the Brain Stimulation Study

In our simulations, we assumed the ultrasound was a plane-travelling wave to simplify the particle velocity vector induced by the oscillation of ultrasound. Experimentally, a “piston” transducer was used, and we operated the experiments in its far field, so the assumption of a plane-travelling wave was valid. However, the particle velocity vector field and the relationship between pressure of ultrasound and particle velocity would be much more complicated when a focused ultrasound transducer should be used. To achieve precise targeting and localization, focused ultrasound combining with a magnetic field is to be studied and explored numerically and experimentally in future works.

In our study, we used a rather small-sized electromagnet to generate an oscillating magnetic field in a small volume, compared to the size of a human’s head. Eventually, we expect to develop this technique for brain stimulation, so a device that could produce an oscillating magnetic field in a larger scale would be desirable. In that case, the operating frequency of the magnetic field might need to be changed because the strong, high frequency oscillating magnetic field might induce effects to the brain without an acoustic field.

6.4 Conclusions

In this dissertation, the generation of monopolar acoustic pulses was studied. The design and manufacturing of a new frequency compounding transducer was described and presented. With the monopolar pulses, we were able to decouple the peak positive pulses from the peak negative pulses thus allowing precise spatial and temporal control between successive pulses in an optimized sequence. A new technique “enhanced shock scattering histotripsy” was explored

and its feasibility was tested. Also, cavitation thresholds at pressure-release interfaces were measured and evaluated. The thresholds were then compared to the intrinsic threshold in free water. Finally, preliminary results were presented regarding an innovative method to achieve neural stimulation with simultaneous ultrasound and oscillating magnetic field.

Appendix: Impedance Tests and Element Construction Details

To choose proper materials as the matching layers for the construction of individual elements for the frequency compounding transducer, impedance tests were performed on various 3-D prototyping materials. Results of the test are shown in Table A.1.

Table A.1 Impedance tests results.

Materials	Speed of sound (m/s)	Density (kg/m^3)	Impedance (MRayl)
FR-4	3086.5	2.02×10^3	6.23
SLS materials			
PA 620 MF	2062.5	1.20×10^3	2.48
PA 850 Black	2325.0	1.03×10^3	2.40
PA 650	2145.4	1.02×10^3	2.19
PA 615 GS	2424.1	1.49×10^3	3.61
SLA materials			
Accura ClearVue Free	2563.6	1.15×10^3	2.95
Accura Xtreme White	2656.0	1.18×10^3	3.13
Accura 60	2668.3	1.21×10^3	3.23
Somos 9120	2425.2	1.16×10^3	2.81
Somos NanoTool 20L	3124.3	1.65×10^3	5.16
Somos WaterShed XC 11122	2504.5	1.16×10^3	2.91
Somos ProtoTherm 12120 (red)	2798.1	1.18×10^3	3.30
RenShape SL 7820 (black)	2535.4	1.16×10^3	2.94

The detailed structure of the individual elements at various resonant frequencies is shown in Table A.2. “Pz 36 HP” means that the disk was the high porosity version of the Pz 36 material, which has an acoustic impedance of 14.5 MRayl. The normal Pz 36 material has an acoustic impedance of 22.8 MRyal.

Table A.2 Structural details of the individual elements at various resonant frequencies.

Frequency	Structure details
250 kHz	Element: 2*500 kHz Pz 36 HP elements stacking; First matching layer: Somos NanoTool; Second matching layer: Somos 9120.
500 kHz	Element: 2*1 MHz Pz 36 HP elements stacking; First matching layer: Somos NanoTool; Second matching layer: Somos 9120.
750 kHz	Element: 1*750 kHz Pz 36 normal element; First matching layer: FR-4; Second matching layer: Somos 9120.
1 MHz	Element: 1*1 MHz Pz 36 HP element; First matching layer: Somos NanoTool; Second matching layer: Somos 9120.
1.5 MHz	Element: 1*1.5 MHz Pz 36 HP element; First matching layer: Somos NanoTool; Second matching layer: Somos 9120.
2 MHz	Element: 1*2 MHz Pz 36 HP element; First matching layer: Somos NanoTool; Second matching layer: Somos 9120.
3 MHz	Element: 1*3 MHz Pz 36 HP element; First matching layer: Somos NanoTool; Second matching layer: Somos 9120.